



UNIVERSITY OF
CAMBRIDGE

Department of Engineering

Propulsion Systems for VTOL Electric Vehicles

Author Name: Megan McEveley

Supervisor: Dr. James Taylor

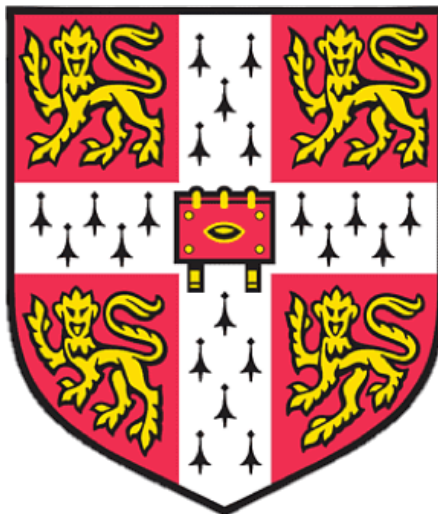
Date: 27/05/2020

I hereby declare that, except where specifically indicated, the work submitted herin is my own original work.

Signed M. McEveley date 27/05/2020

Propulsion Systems for VTOL Electric Vehicles

Report submitted to
The Cambridge University Engineering Department
27th May 2020



Megan McEveley

Supervised by
Dr. James Taylor

Abstract

For electric vertical take-off and landing (eVTOL) vehicles there are two options for propulsor design: propellers, or ducted fans. The performance of eVTOL vehicles is quantified using a non-dimensional figure of merit. A literature review shows ducted fans to theoretically excel in hover performance over propellers, with a 40% greater value in figure of merit. However, ducted fans are not as frequently used as propellers in commercial eVTOL vehicles due to the complexity of their design; the inlet and exit ducts must be optimised for both weight and performance. If the duct has separation, it can cause the ducted fan to perform worse than a propeller.

In this work, the influence of the inlet and exit duct geometry design on separation and the overall performance of ducted fans in hover is investigated. Two methods are discussed which have been developed to investigate and compare the performance of different ducted fan designs in detail, the first using computational fluids dynamics (CFD) and the second, an experimental test rig.

The first section of results provides an understanding of the effect of inlet duct geometry on fan performance. An inlet geometry based on a quarter ellipse ensures smooth curvature changes. The inlet performance can be improved in two ways. The first by reducing the length, this increases the net thrust by decreasing both dissipation and weight. The second by using a relatively large inlet diameter. This reduces both the initial curvature of the inlet and the incidence of the oncoming flow, preventing separation.

The second section of results focuses on exit duct geometry. The area ratio of the exit duct is critical in setting the operating point and performance of a ducted fan. Exit ducts with area ratios ranging from 1.00 to 2.05 were tested and analysed using CFD. Increasing the area ratio of the exit duct was found to increase the figure of merit up until the exit duct began to show significant separation. The highest performing exit duct had an area ratio of $\sigma = 1.69$, increasing the figure of merit by 21% when compared to an exit duct with an area ratio of 1.00.

Separation of the exit duct was found to be detrimental to ducted fan performance in two ways. First, it reduced the actual area ratio of the flow through the ducted fan, changing the operating point and reducing the figure of merit. Second, the separation increased losses, further reducing the figure of merit.

Shortening the exit duct geometry, whilst maintaining the same geometric area ratio, leads to more aggressive diffusion and separation. A reduction of 50% in duct length caused a decrease in figure of merit of 9.9%. CFD showed that this separation could be prevented, and the figure of merit improved with the use of a splitter blade. With a splitter blade, a reduction of 50% in duct length led to a decrease in figure of merit of only 2% when compared to the long exit duct.

When tested on the experimental rig, the ducted fan geometries were found to differ in performance to the CFD results. First, CFD was found to be conservative when estimating separation. Second, the flow through a ducted fan was found to be sensitive to 3D geometry. Swirl can influence the separation of the exit duct and incidence of the exit flow out of the stator can also lead to separation on the splitter blade. The duct can be redesigned and optimised to prevent these problems.

Acknowledgements

The author would like to thank Dr. James Taylor and Dr. Sam Grimshaw for their invaluable guidance and ongoing support throughout this project. Thanks also to the research staff who have shared their knowledge of aerodynamics and to the technicians of the *Whittle Laboratory* for their assistance in the workshop.

Contents

| | | |
|-----------|--|-----------|
| 1 | Introduction | 5 |
| 1.1 | Background & Motivation | 5 |
| 1.2 | Literature Review | 5 |
| 1.3 | Project Aims | 8 |
| 1.4 | Approach | 9 |
| 2 | Numerical Methods | 10 |
| 2.1 | Ducted Fan Geometry | 10 |
| 2.2 | Turbomachinery Grid Generation | 10 |
| 2.3 | Inlet and Exit Duct Grid Generation | 11 |
| 2.4 | TURBOSTREAM | 12 |
| 3 | Experimental Methods | 12 |
| 3.1 | Test Rig Setup | 12 |
| 3.2 | Instrumentation | 12 |
| 4 | Analysis Methodology | 16 |
| 4.1 | Control Volume Analysis | 16 |
| 5 | The Effect of Inlet Duct Geometry on Separation | 18 |
| 5.1 | Inlet Duct Geometry Results | 18 |
| 5.2 | Inlet Duct Splitter Results | 21 |
| 6 | The Effect of Exit Duct Geometry on Performance | 22 |
| 6.1 | Exit Duct Geometry | 22 |
| 6.2 | CFD Results | 23 |
| 6.3 | Experimental Results | 29 |
| 7 | The Effect of Splitter Blades on Exit Duct Length | 32 |
| 7.1 | Splitter Blade Design | 32 |
| 7.2 | CFD Splitter Blade Performance | 32 |
| 7.3 | Experimental Splitter Blade Performance | 35 |
| 8 | Sensitivity to 3D Geometry | 37 |
| 8.1 | Splitter Blade Performance | 37 |
| 8.2 | Location of Exit Duct Separation | 41 |
| 9 | Main Steps in Ducted Fan Design | 42 |
| 10 | Conclusions | 43 |
| 10.1 | Future Work | 43 |
| | Appendices | 45 |

Nomenclature

Geometry

σ Exit duct area ratio

θ Diffuser angle

A_{pass} Fan passage area

AR Aspect Ratio

c_x Axial chord length

D Diameter

h Fan hub to casing length

L Exit Duct Length

Other

\dot{m} Total mass flow

Λ Reaction

ϕ Flow coefficient

ψ Stage loading coefficient

C_p Static pressure coefficient

c_p Specific heat capacity

C_{po} Total pressure coefficient

M_f Non-dimensional figure of merit

P Electrical Power

T Thrust

U Blade speed at meanline

M Mach Number

Subscripts

$()_0$ Upstream Far-Field

$()_1$ Upstream Inlet Duct

$()_2$ Downstream Inlet Duct

$()_3$ Upstream Exit Duct

$()_4$ Downstream Exit Duct

$()_5$ Downstream Far-Field

$()_r$ Rotor

$()_s$ Stator

$()_x$ Axial

$()_{cas}$ Fan Duct Casing

$()_{gap}$ Rotor blade tip gap

$()_{geom}$ Geometric

$()_{ND}$ Non-dimensional

Abbreviations

APG Adverse pressure gradient

CFD Computational fluid dynamics

ESDU Engineering Sciences Data Unit

eVTOL Electric vertical take-off and landing

FDM Fused Deposition Modelling

PAV Passenger air vehicle

RANS Reynolds-averaged Navier–Stokes

UATs Urban air taxis

UAVs Unmanned aerial vehicles

UROP Undergraduate Research Opportunities Programme

1 Introduction

This project investigates the use of ducted fans as the propulsor for eVTOL vehicles. The project aim is to demonstrate how ducted fan power consumption can be reduced by optimising the duct geometry to be efficient and lightweight.

1.1 Background & Motivation

Two of the main markets of eVTOL vehicles are unmanned aerial vehicles (UAVs) and urban air taxis (UATs). UAVs can be used in applications such as aerial recognition, package deliveries and monitoring agriculture [1]. The UAV market is estimated to more than double in the next 6 years, with the rise in the procurement of military UAVs by defence forces worldwide having a significant influence [2]. There is also growing interest in the UAT market as an alternative mode of transport which does not require expensive infrastructure and could help to reduce traffic congestion. With these markets of eVTOL vehicles growing, improving the efficiency is an important factor when wanting to extend the range of flight.

The transport sector contributes 33% of the UK's CO₂ emissions [3]. Research has shown that over a distance of 100km, eVTOL vehicles can produce 35% less greenhouse gas emissions compared to gas- or diesel-powered road vehicles due to better cruise performance [4]. If efficiency in hover during take-off and landing could be improved, this reduction in emissions could be seen over shorter distances as well. Improving hovering efficiency is therefore important as it would enable eVTOL vehicles to be a more practical alternative mode of transport whilst helping to reduce CO₂ emissions of the transport sector.

1.2 Literature Review

This literature review compares the advantages and limitations of ducted fans over other propulsor types used in the eVTOL market. Existing methods to establish ducted fan performance in terms of separation and efficiency are then discussed. Finally, splitters are investigated as a way of reducing ducted fan weight.



(a) Aurora Pegasus propeller eVTOL UAT



(b) CAD of a ducted fan eVTOL UAT

Figure 1: Propeller and ducted fan eVTOL vehicles [5]

1.2.1 Ducted Fans

The two main propulsor types for eVTOL vehicles are propellers, where the rotor blades are open, Fig. 1a, and ducted fans, where a cylindrical shroud or duct surrounds the rotor, Fig. 1b. Propellers have been adopted in many eVTOL designs and proven to work successfully, whereas ducted fans are seen less frequently.

It has been found that ducted fans, when compared to propellers, have significant gains in aerodynamic performance and operability. The first is an increase in thrust on the nacelle; Lipera found that the duct of the iSTAR Micro Air Vehicle ‘increases propulsion efficiency and produces lift in horizontal flight, similar to a conventional planar wing’ [6]. Second, the addition of a duct reduces the intensity of tip vortices. This leads to a reduction in tip losses and increases the efficiency of the fan. As well as this, diminishing tip vortices leads to reduced noise pollution which is vital in urbanised areas and in military applications. A second contribution to fan noise also comes from the jet at the exit of a fan, but the use of a duct allows the jet geometry to be modified and the exit flow to be diffused, reducing jet noise [7]. Third, ducted fans are inherently safer as the blades are contained by the duct in the event of blade-off. The blades themselves are also protected from damage in impacts.

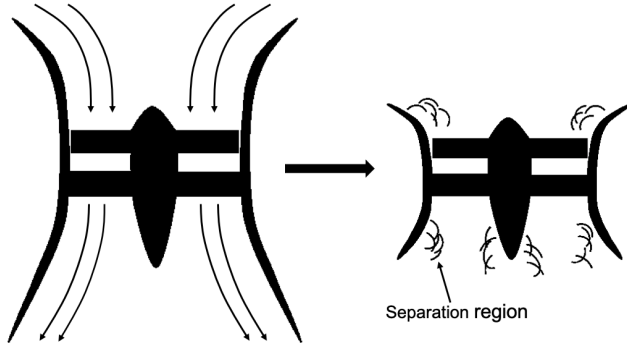


Figure 2: Separation regions of a short ducted fan

Despite these advantages, the performance of a ducted fan can be limited by separation. Separation can be due to two reasons, the first being crosswinds which can cause the flow to separate off the inlet duct. The second is duct length. It is desirable to have lighter ducts to increase the net thrust. The duct can be made lighter by shortening its length, but this also leads to aggressive flow turning and separation, as shown in Fig. 2.

Separation is detrimental to the overall performance of a ducted fan as it increases aerodynamic losses, reducing efficiency. Separation is also detrimental to the performance of individual sections of the ducted fan. Separation of the inlet leads to inlet flow distortion which causes instability and degrades the fan operating range, leading to early stall [8]. Separation of the exit causes the fan to operate at a different point to its design, reducing its efficiency. The prevention of separation is therefore important in improving the performance of ducted fans.

1.2.2 ESDU Performance Charts

The area ratio of the exit duct is defined as the ratio of area downstream to the area upstream. For eVTOL vehicles in hover, it is desirable to diffuse the exit flow as much as possible to improve the propulsive efficiency. However, increasing the area ratio increases the adverse pressure gradient and separation becomes more likely.

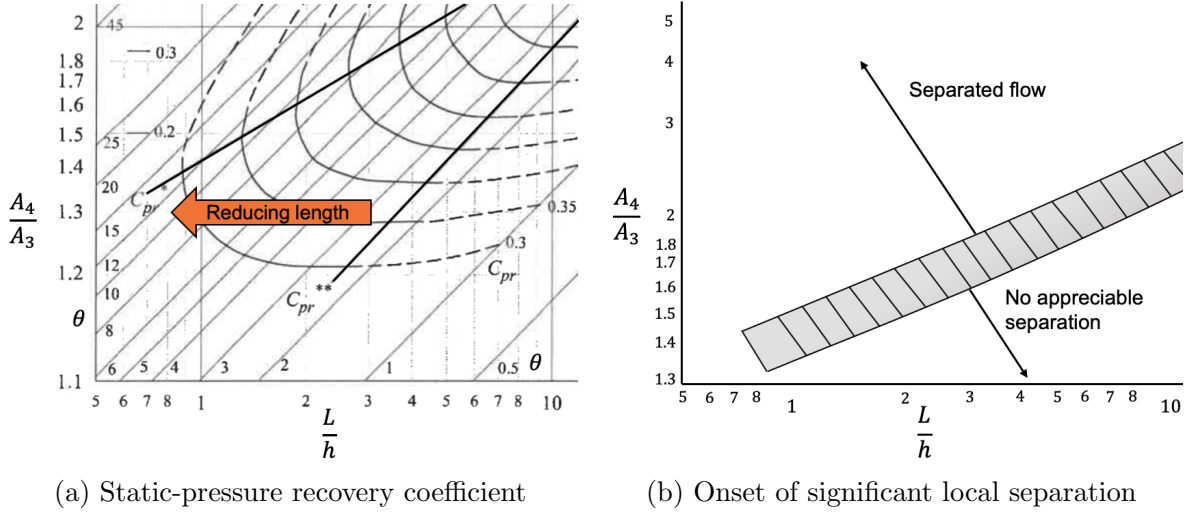


Figure 3: ESDU performance charts for symmetrical annular diffusers, adapted from [9]

Two different performance charts for circular annular diffusers in incompressible flow are given in ESDU 75026 [9]. The first performance chart provides values of static-pressure recovery coefficient, Fig. 3a, where the C_{pr}^* line shows optimum area ratios for given length and wall angles. The second performance chart shows the limit for separation, Fig. 3b. C_{pr}^* values correspond to the separation limit of different duct geometries. The ESDU charts show that longer ducts can achieve higher area ratios without separation. The charts can therefore be used to assist in the design of an exit duct geometry with no appreciable separation.

1.2.3 Figure of Merit for Propulsor Performance

Whilst the separation limit of an exit duct is important, it does not quantify ducted fan performance. Efficiency is difficult to define in hover; therefore, a different performance metric is required to compare the performance of fan designs. The Hiller Aircraft Corporation have defined a non-dimensional figure of merit [10], characterising the efficiency of a propulsor, as in Equation (1).

$$M_f = \frac{T_{Total}}{P} \sqrt{\frac{T_{Total}}{2\rho A_{pass}}} \quad (1)$$

A high figure of merit means less power consumed during a flight mission. Applying simple momentum theory to both a propeller and a ducted fan with no diffuser, the figure of

merit value for each configuration is 1.00 and 1.41 respectively [11]. If problems of separation can be overcome, ducted fans offer a reduction in power of 40% for the same propulsor disc area.

By changing the exit duct geometry to a diffuser with area ratio σ , control volume analysis and momentum theory can be used to theoretically predict how the figure of merit scales with σ . This results in Equation (2). The aim of this project is to investigate how σ can be maximised to maximise figure of merit.

$$M_{f, \text{ducted}} = \sqrt{2\sigma} \quad (2)$$

1.2.4 Splitter Blades

Splitters are circumferential blades which help to turn the flow and keep boundary layers attached, shown in Fig. 4. Splitter blades are often adopted in the design of centrifugal compressors as they allow a reduction in wetted area whilst preventing separation in the rotor and maintaining solidity [12]. More recently, splitter blades have been used to control the secondary flows in an axial turbine blade row with low aspect ratio vanes as they split the diffusion of highly loaded components. They were found to improve the stage efficiency by 0.88% compared to a design without splitter blades [13]. Splitters at inlet and exit could enable a shorter and lower weight duct whilst preventing separation and maintaining a high figure of merit.

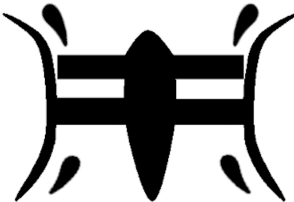


Figure 4: Splitters on the inlet and exit ducts of a short ducted fan

1.3 Project Aims

The aim of the project is to address the challenges of ducted fans for eVTOL vehicles and improve their hovering efficiency whilst reducing their weight. The specific questions investigated in this project are:

1. How can separation on the inlet be prevented?
2. How does exit duct geometry affect propulsor performance?
3. How can the exit duct be made shorter and lighter?

1.4 Approach

This project is a continuation of the work conducted last year by J. Barry, which saw the successful completion of a ducted fan test rig capable of measuring thrust, power and shaft speed. However, it was found that more detailed analysis of the flow was required to design an optimum ducted fan. In a UROP completed by the author last summer, Autogrid was used to mesh the ducted fan blading.

In this project, two methods have been developed and used to investigate the flow in ducted fans and evaluate the performance of different designs. Different designs are compared by their figure of merit and so both methods need to be capable of evaluating it. The first method is the use of computational fluid dynamics (CFD) that has been developed to model the flow through the ducted fan, this involved the blading mesh from the UROP as well as producing new meshes for the duct geometry. The second method involved the use of the eVTOL test rig and the addition of further instrumentation to validate new duct geometries experimentally. These methods are given in Section 2 and 3, respectively.

For detailed analysis of the ducted fan, it must be broken down into components to ensure each component is performing as designed. Control volume analysis can be used to break down the ducted fan, as described in Section 4.

The inlet section of a ducted fan can produce significant amounts of thrust. The effect of changing the inlet geometry to reduce its weight whilst maintaining its thrust is considered in Section 5.

The influence of exit duct geometry and diffusion is investigated in Section 6. Section 6.2 describes the influence of exit duct geometry on separation and the figure of merit using CFD, with Section 6.3 comparing these findings with experiment.

In Section 7, splitter blades are introduced to the exit duct geometry to characterise the effect on separation. Discrepancies between CFD and experimental findings are then investigated in Section 8.

2 Numerical Methods

CFD was used for ducted fan analysis as it allows for geometry adjustments to be made to the inlet and exit of the ducted fan and for their impacts to be analysed quickly and cheaply. CFD also enables full access to the flow and the ability to look at specific features in detail.

2.1 Ducted Fan Geometry

The ducted fan is made up of three parts, the inlet, the turbomachinery fan section and the exit duct, Fig. 5. The turbomachinery blading of the ducted fan was designed in a previous project using a blade geometry script developed for low Reynolds number compressors [14]. Velocity triangles were drawn at the hub, mid radius and casing and vectorised to give parameters for each spanwise position. This resulted in a fan of 11 rotor blades and 13 stator blades. The inlet geometry is a smooth hyperbolic curve to reduce separation. The exit of the ducted fan is designed using the ESDU charts for symmetrical, annular diffusers [9], with linear, constant angle duct and exit cone geometries. This is discussed further in Section 6.1.

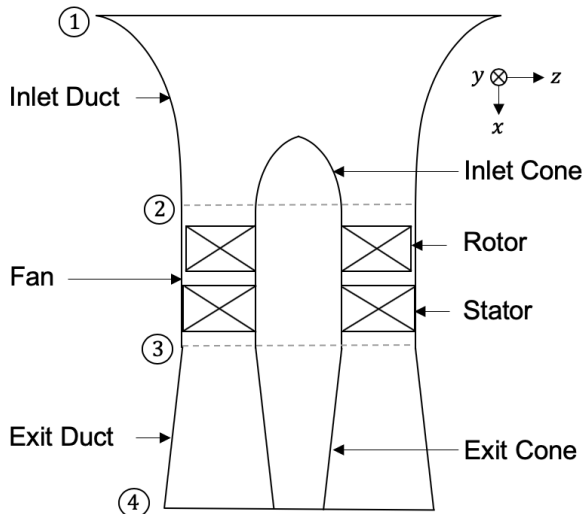


Figure 5: Annotated sections of the ducted fan

2.2 Turbomachinery Grid Generation

Autogrid was used to mesh the turbomachinery section of the ducted fan. The nodes are clustered at the cell walls with a y^+ value of 1.2. Goodhand & Miller (2012) describe how the effect of fillet radius is of secondary importance and that this has insignificant influence on the flow as long as it is not removed [15]. For this reason, to improve the mesh quality, the hub fillet radius used in the mesh was larger than that used in the experimental rig. The

tip gap and inter-platform gaps were fully meshed. The blading mesh consists of a total of 930,000 cells. The 2D mesh of the turbomachinery blades is shown in Fig. 6.

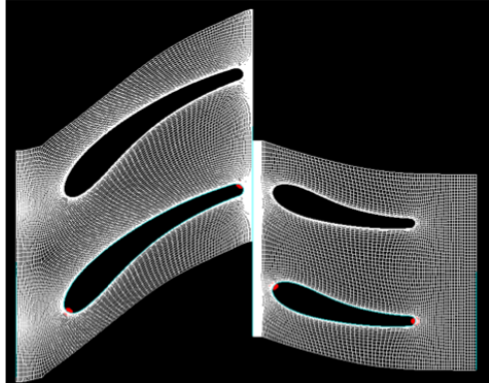


Figure 6: 2D cross-section of the turbomachinery blading mesh

2.3 Inlet and Exit Duct Grid Generation

The duct geometry was created as a structured 2D mesh in Pointwise. Due to the low Mach number of the flow through a ducted fan in hover, the CFD is extremely sensitive to the boundary conditions applied to the blocks. Different combinations were tried, and the best was found to be a curved inlet boundary, as shown in Fig. 7.

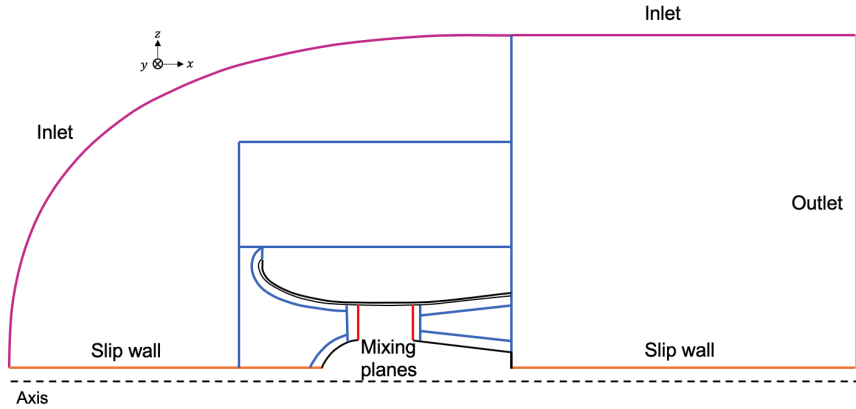


Figure 7: 2D Pointwise mesh of the duct geometry with boundary conditions labelled

Nodes are clustered near solid walls, in this case along the surface of the cones and inlet and exit ducts. The flow through the fan is assumed axisymmetric and the 2D duct geometry spans a 10-degree sector to form the block domain. The inlet and outlet meshes do not reach zero radius as the CFD works in polar coordinates, instead, a slip wall is applied as shown in Fig. 7. This approximation is suitable if the flow is axisymmetric. The Pointwise mesh consists of a total of 490,000 cells.

2.4 TURBOSTREAM

The Pointwise duct and Autogrid blading meshes are coupled together with a mixing plane, which takes a meridional average of the pressure field produced by the fan. TURBOSTREAM was used to solve the flow through the fan by running RANS simulations, further details are given in Ref. [16]. The mixing length turbulence model was used for robustness and speed [17].

3 Experimental Methods

The eVTOL rig was used in this project to test different ducted fan designs experimentally. CFD can struggle to predict separation accurately and should be calibrated by comparison with test data as frequently as possible [18]. To investigate separation in detail, further instrumentation was added to the rig as described in Section 3.2.2.

3.1 Test Rig Setup

The design of the test rig allows for different inlet and exit duct designs to be easily fitted and replaced. All components of the ducted fan are 3D printed, with the inlet and exit ducts split into 4 parts, allowing them to be printed on most common FDM 3D printers. The eVTOL rig is small scale with tight clearance of the rotor blades to the casing. For this reason, it must be carefully clocked and balanced before running. Table 1 shows the operating point and geometry of the fan section of the rig. The 3D printed fan section of the rig is shown in Fig. 8a.

| Parameter | Value | Parameter | Value |
|-----------|-------------------|-------------------|--------|
| ϕ | 0.6 | r_{hub}/r_{cas} | 0.458 |
| ψ | 0.7 | $t_{gap}/chord$ | 0.007 |
| Λ | 0.825 | AR_r | 1.8 |
| Re | 2.2×10^5 | AR_s | 1.8 |
| M | 0.081 | D_{cas} | 240 mm |

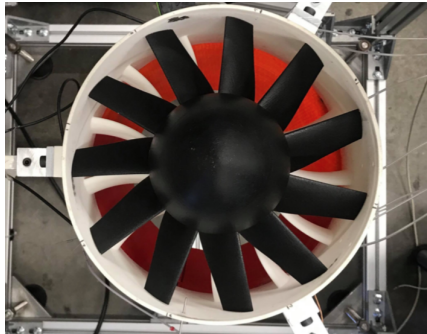
Table 1: Rig operating point and geometry

3.2 Instrumentation

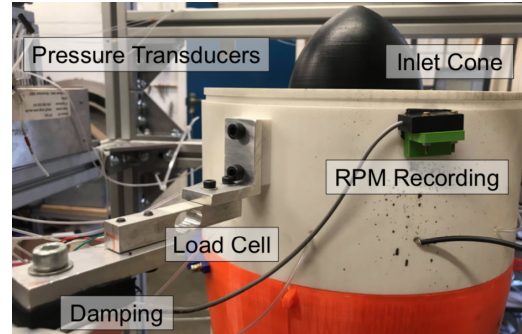
The purpose of the rig is to test and validate ducted fan designs against the CFD results. Therefore, it must be capable of measuring figure of merit to validate 1D performance. It must also be able to evaluate the inlet and exit duct independently to break down the analysis and establish how well each part of the ducted fan is performing.

3.2.1 Figure of Merit Measurement

To obtain a value for the figure of merit of a duct, three measurements are required: a speed measurement to set the fan at its operating point and thrust and power measurements for calculation. Shaft speed is recorded using a once-per-revolution infra-red optical sensor. The power is measured directly by the external power supply as an analog output voltage.



(a) 3D printed eVTOL fan blading



(b) Rig instrumentation

Figure 8: eVTOL test rig

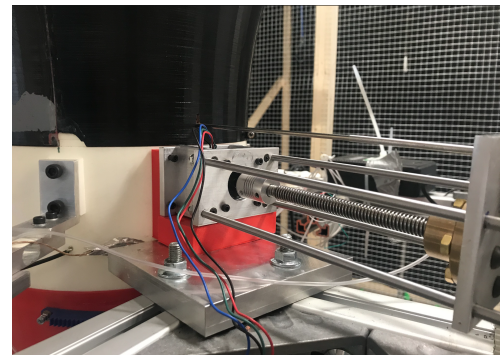
The ducted fan is mounted to three identical loads cells to ensure stiffness matching of the supports and prevent vibration, with one load cell used to measure the total thrust, shown in Fig 8b. Trial weights were used to calibrate the load cell and plot a linear characteristic. The load cell readings drift with temperature and so the zero reading of the load cell is logged before each run.

3.2.2 Inlet and Exit Duct Performance Measurements

In this project, further instrumentation has been added to the rig to make intermediate measurements and characterise the performance of the inlet and exit ducts.



(a) 2D traverse downstream of the exit duct



(b) Radial traverse at inlet to the rotor

Figure 9: eVTOL test rig traverses

A five-hole probe was added to the rig to perform area traverses upstream and downstream of the ducted fan, as well as radially at the inlet to the rotor. The five-hole probe is capable of measuring static pressure, stagnation pressure, yaw angle and pitch angle relative to the probe head. The five-hole probe traverse data can be used to identify flow features or determine flow properties for loss analysis. It can also be numerically integrated for thrust analysis, as described in Appendix A.

For upstream and downstream, a 20×20 Cartesian grid was traversed using two stepper motors, allowing for repeatable traverse points with accurate and automated movements, Fig 9a. Speedframe allowed the traverse to be easily transferred between upstream and downstream and dowel pins were used to ensure correct alignment of the probe as it was moved between the different traverse types. For the radial traverse, a bracket was 3D printed to connect a stepper motor to the casing of the fan, positioning the probe at inlet to the rotor. This allowed for a 1D radial traverse from casing to hub of the flow with clustering at the walls. The radial traverse is shown in Fig. 9b.

For accurate measurements the probe must be calibrated using known flow angles to produce a grid of calibrated points. Dominy and Hodson (1993) describe the four coefficients used for calibration [19]. The calibration surfaces are plotted in Fig. 10.

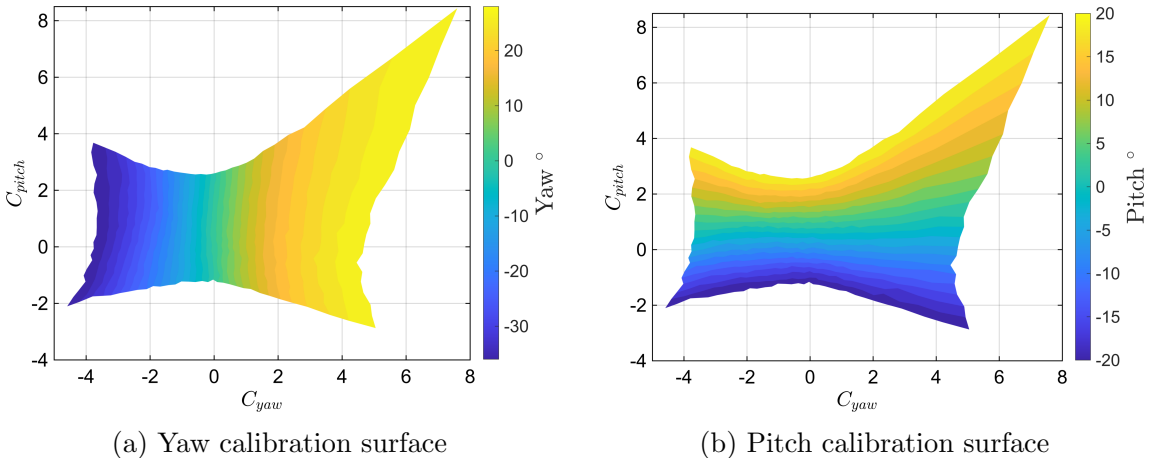


Figure 10: Calibration surfaces

The probe settling time was optimised as described in Grimshaw and Taylor (2016) and set to 1.2 s [20]. The diameter of the probe head is 1.3 mm which is equivalent to 1.08% of the duct span. A 16-port pressure scanner is used to record the five-hole probe readings as well as data from static pressure tappings placed along the surfaces of the inlet and exit ducts to calculate the individual thrust components. This provides accurate pressure readings within 0.07% of the dynamic head.

3.2.3 Mass Flow Calibration

To test different duct geometries efficiently and quickly, a dimensional calibration factor, K can be calculated, Equation (3), to provide the calibrated inlet mass flow, as described by Dunkley (1998) [21]. This means that a radial traverse at inlet to the rotor does not need to be performed for every duct geometry.

$$K = \int \frac{\rho_{pr} V_{x,pr}}{\sqrt{\rho_2(p_{02} - p_2)}} dA \quad (3)$$

where ρ_{pr} and $V_{x,pr}$ are the density and axial velocity measured by the five-hole probe. p_{02} and ρ_2 are the stagnation pressure and density at inlet to the rotor, respectively. p_2 is the static pressure at inlet to the rotor, measured using a static pressure tapping. The mass flow into the fan is then given by Equation (4).

$$\dot{m}_{in} = \sqrt{\rho_2(p_{02} - p_2)} K \quad (4)$$

Static pressure measurements were to be taken in the next stage of the project, allowing K to be calculated, see Appendix E.

4 Analysis Methodology

4.1 Control Volume Analysis

To investigate the performance of the individual ducted fan sections, a thrust breakdown is required. The total thrust of the ducted fan is made up of three components; the thrust from the inlet, the thrust from the turbomachinery fan section and the thrust from the exit.

$$T_{Total} = T_{Inlet} + T_{Fan} + T_{Exit} \quad (5)$$

Control volumes can be applied to both the CFD analysis and the experimental rig to find the total thrust and thrust contributions from each section. In the CFD, cuts at locations 1 through to 4 can be applied to find the exact axial velocity. For measurements made on the rig, the axial velocity across the fan section is assumed constant as this is what the turbomachinery is designed for in the ideal case. From continuity, the mass flow through the fan should be constant, however the CFD allows the mass flow at each of locations 1 to 4 to be calculated and the five-hole probe measurements of the rig allow the mass flow at 1, 2 and 4 to be calculated exactly.

Applying the steady flow momentum equation to a control volume around the whole fan gives Equation (6).

$$T_{Total} = \dot{m}(V_j - V_0) = \dot{m}V_j \quad (6)$$

The inlet control volume is shown in Fig. 11. Applying the steady flow momentum equation to the inlet section gives Equation (7) for the inlet thrust. Since the pressure is atmospheric far upstream of the inlet, the pressure term in Equation (7) reduces to the gauge pressure at inlet to the rotor multiplied by the flow area at inlet to the rotor.

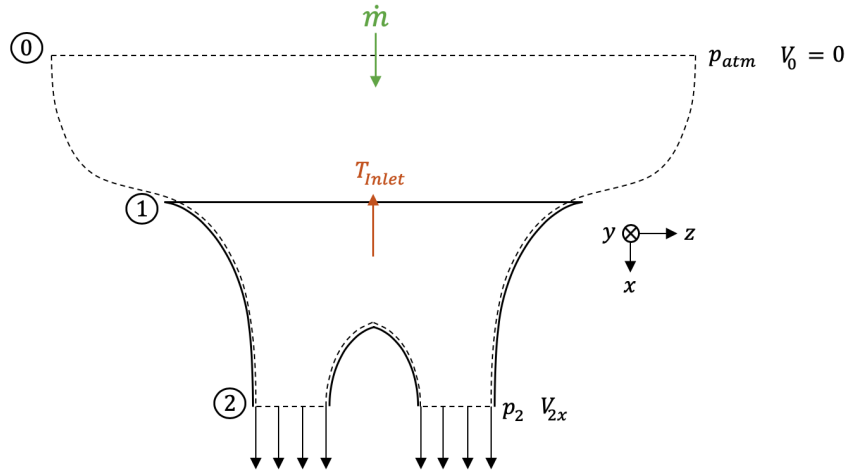


Figure 11: Inlet duct control volume

$$T_{Inlet} = \dot{m}V_{2x} + (p_2 - p_{atm})A_{pass} \quad (7)$$

Alternatively, the thrust on the rig can be found directly from the static pressure tappings on the duct, which measure the gauge pressure at evenly spaced points along the inside duct surface, and using integration to find the forces, Equation (8). A similar approach can be applied in the CFD by taking a cut along the surface of the duct, extracting the pressure at each point along the cut and then integrating with respect to the area. Further details of this can be found in Appendix B.

$$T_{Inlet} = [pA]_{Inlet} + [pA]_{Inlet\ Cone} \quad (8)$$

Across the fan, it is not possible to put pressure tappings along the blades, so here the steady flow momentum equation is used, this gives Equation (9).

$$T_{Fan} = \dot{m}V_{3x} - \dot{m}V_{2x} + (p_3 - p_2)A_{pass} \quad (9)$$

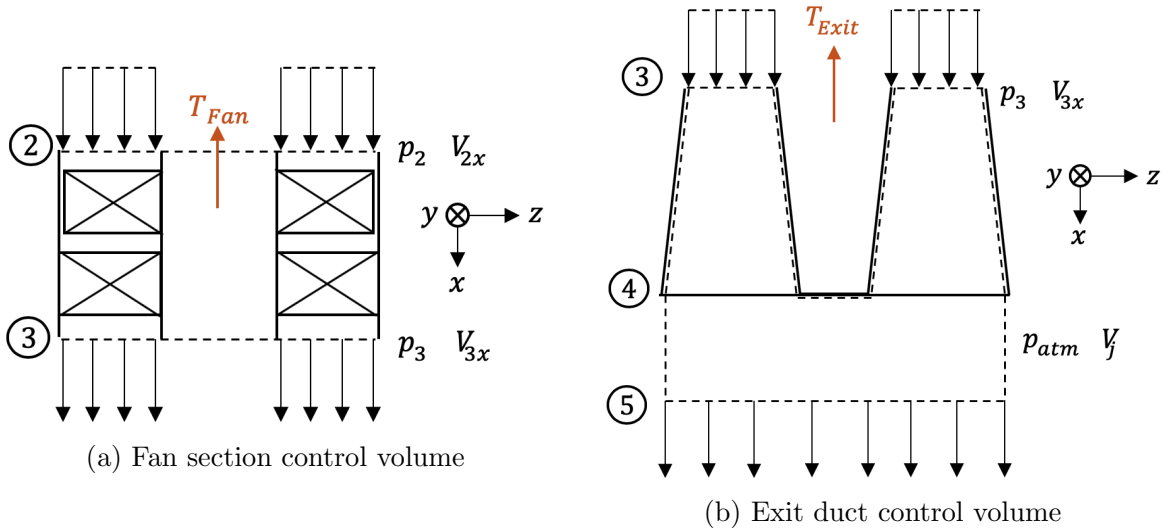


Figure 12: Fan and exit duct control volumes

For the exit duct, the control volume shown in Fig. 12b is used, where V_j is the axial component of the jet velocity. In the CFD, the axial component of the jet velocity can be extracted from the cuts. For measurements taken on the eVTOL rig, the axial jet velocity component is calculated using the yaw and pitch angles of the flow. Using this control volume, the steady flow momentum equation can be applied to give Equation (10). Alternatively, numerical integration can be used along the exit duct surface to calculate the surface pressure forces, Equation (11).

$$T_{Exit} = \dot{m}V_j - \dot{m}V_{3x} + (p_{atm} - p_3)A_{pass} \quad (10)$$

$$T_{Exit} = [pA]_{Exit} + [pA]_{Exit\ Cone} \quad (11)$$

5 The Effect of Inlet Duct Geometry on Separation

To investigate separations at the inlet, three ducts of different size were tested using CFD with the same exit duct geometry. Splitters were then added to the inlet to investigate the influence on thrust.

5.1 Inlet Duct Geometry Results

The inlet geometry was designed using a quarter segment of an ellipse, with semi-major axis a and semi-minor axis b . The inlet geometry is shown in Fig. 13.

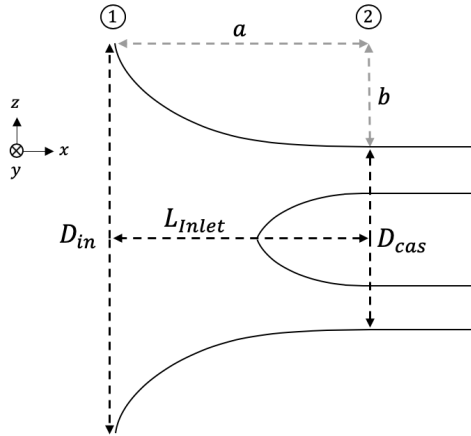


Figure 13: Inlet duct geometry

5.1.1 CFD Results

The first inlet tested using CFD was a long baseline inlet, Inlet 1. This inlet was then scaled in size in two ways. First, its length was scaled, Inlet 2, to reduce weight. Second, both the datum length and inlet diameter were scaled, Inlet 3, further reducing weight but also reducing drag in forward flight. Figure 14 shows contours of flow coefficient for each inlet design.

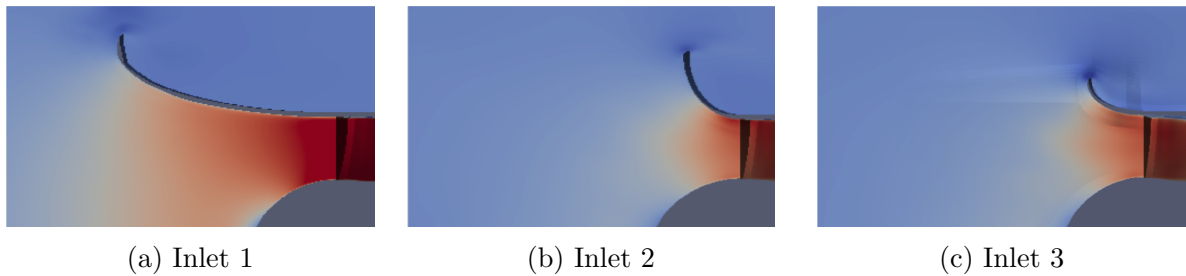


Figure 14: Contours of flow coefficient for inlet ducts tested using CFD

From Fig. 14, it can be seen that there are no re-circulation regions on either of the inlets and therefore, the flow has remained attached in all three cases. This suggests that an elliptical shaped inlet turns the flow gradually enough to prevent separation.

Figure 15 shows the streamlines of the flow over Inlet 2 with contours of static pressure. The flow accelerates along the inlet surface, creating a low-pressure region on the convex side. Behind the inlet duct is a slowly recirculating region with pressure equal to atmospheric pressure. The difference generates the thrust of the inlet duct.

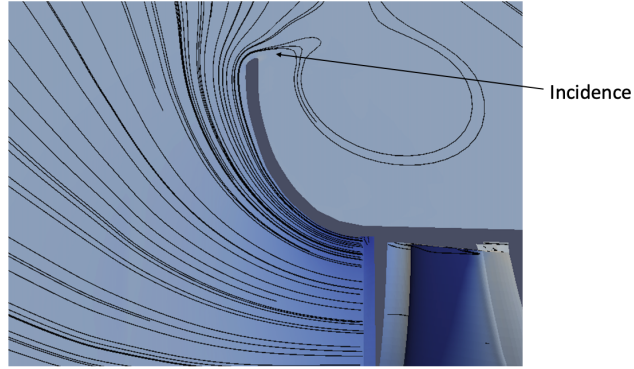


Figure 15: Streamlines of Inlet 2 with contours of static pressure

The non-dimensional thrust of each inlet tested using CFD is recorded in Table 2, where thrust is non-dimensionalised using the design axial velocity, Equation (12).

$$T_{ND} = \frac{T}{\frac{1}{2}\rho V_x^2 A_{pass}} \quad (12)$$

| Inlet Duct | L_{Inlet}/D_{cas} | D_{in}/D_{cas} | Inlet T_{ND} |
|------------|---------------------|------------------|----------------|
| Inlet 1 | 0.833 | 1.583 | 0.772 |
| Inlet 2 | 0.208 | 1.583 | 0.800 |
| Inlet 3 | 0.208 | 1.292 | 0.748 |

Table 2: Thrust produced by different inlet ducts tested using CFD

Theoretical control volume analysis predicts the thrust to be equal for all inlets since they have equal inlet exit areas and the same exit ducts to ensure that they are operating at the same mass flow. The results of the CFD agree well with theory as the thrusts of the inlets are within 7% of each other.

The small difference in thrusts is due to viscosity and the growth of boundary layers influencing the inlet duct performance. Reducing the inlet length from Inlet 1 to Inlet 2 improved the inlet performance the most, increasing its thrust by 3.63% from the baseline inlet. Since the length of duct is shorter than the baseline inlet, dissipation is reduced, increasing the mass flow through the duct and therefore, increasing the thrust.

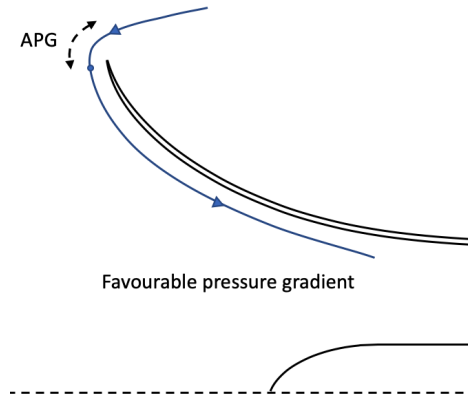


Figure 16: Adverse pressure gradient upstream of the inlet duct

Reducing both inlet length and diameter from Inlet 1 to Inlet 3 reduced the thrust by 3.11% from the baseline. In hover, the inlet flow behaves as a sink and upstream of the inlet there is flow incidence, shown in Fig. 15. Due to the incidence and curvature of the flow over the duct surface, there is an adverse pressure gradient upstream of the inlet, before the flow accelerates and a favourable pressure gradient occurs, shown schematically in Fig. 16. Reducing the inlet diameter increases the curvature upstream of the duct. This leads to a significantly higher adverse pressure gradient, causing the boundary layers to grow quicker. Because of this, Inlet 3 also operated furthest from design as its axial velocity was lower than the other inlets, resulting in a lower mass flow through the fan and a reduced inlet thrust.

5.1.2 Experimental Results

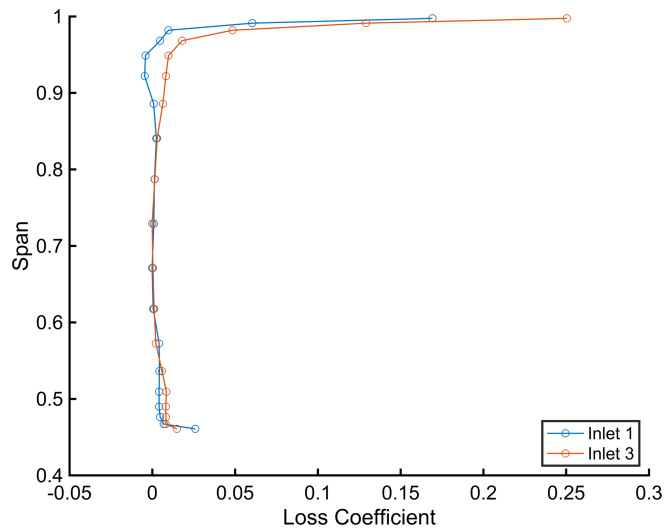


Figure 17: Loss Coefficient of inlet geometries tested on the eVTOL rig

To investigate the poor performance of Inlet 3 further, this inlet was tested on the eVTOL rig as well as Inlet 1. The plot of loss coefficient, Fig. 17, from the experimental results suggests that the flow has potentially separated on the casing of Inlet 3. This is shown by the loss coefficient being 0.02 for Inlet 3 at a span of 0.9. This region is outside of the boundary layer and if the flow was fully attached, the loss coefficient would be expected to be 0.00 here, as in the Inlet 1 case.

The separation of Inlet 3 on the experimental rig shows that whilst CFD is a useful tool for analysing performance, it can be insensitive to flow separation, especially for laminar flow and when strong pressure gradients are present. It is important to align the duct upstream of the inlet with the flow angle by reducing the curvature here. This reduces the flow incidence and the adverse pressure gradient, preventing separation.

5.2 Inlet Duct Splitter Results

A splitter blade was added to the mesh of Inlet 3 and tested using CFD. Figure 18 shows contours of flow coefficient for the splitted inlet.

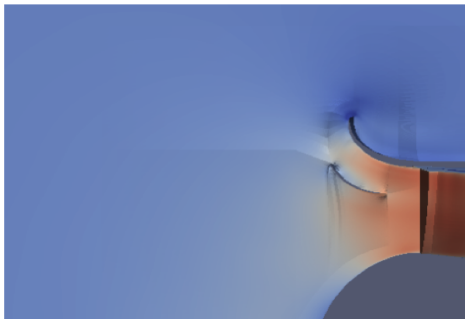


Figure 18: Contours of flow coefficient for Inlet 3 with a splitter blade

The addition of a splitter blade to the inlet reduced the performance, reducing the thrust of Inlet 3 by 9.5%. This is thought to be due to the growth of boundary layers on the splitter blade itself, increasing losses and reducing the mass flow into the ducted fan.

| Inlet Duct | Inlet T_{ND} |
|-----------------------|----------------|
| Inlet 3 | 0.748 |
| Inlet 3 with splitter | 0.677 |

Table 3: The effect of splitters on inlet thrust

Since the CFD did not show any separation on the inlet geometries tested, the addition of the splitter was detrimental to performance. Had separation been present, as in the experiment, the addition of a splitter may have improved performance. In the next stage of the project, a 3D printed splitter for the inlet was to be tested on the eVTOL rig and its influence on loss coefficient and separation analysed, refer to Appendix E.

6 The Effect of Exit Duct Geometry on Performance

6.1 Exit Duct Geometry

The geometries of the exit ducts tested were symmetrical, annular diffusers, shown in Fig. 19, as used in the ESDU charts [9].

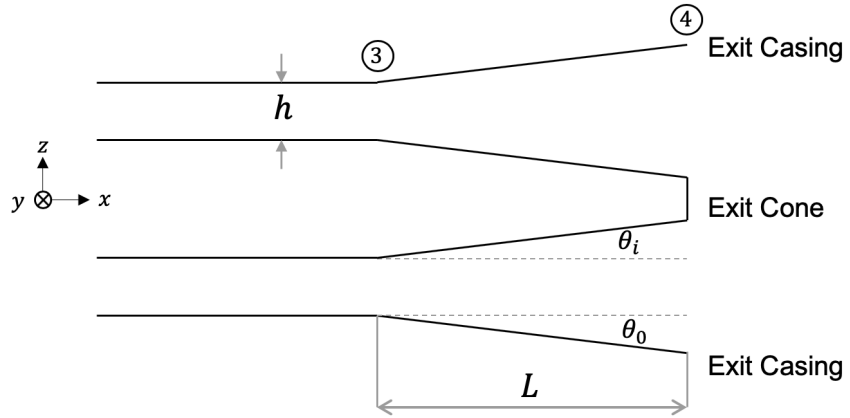


Figure 19: Exit duct geometry, adapted from [9]

The angles θ_i and θ_0 were set to be equal. The area ratio is given by Equation (13).

$$\sigma = \frac{A_4}{A_3} \quad (13)$$

For an exit duct with the same geometry as Fig. 19 and no splitter, the ratio of L/h and the chosen area ratio fixes the angle θ . For the exit ducts tested in this project h is equal to the difference between the casing and hub radius, which is fixed at 65 mm. Therefore, two geometry changes could be investigated: area ratio, and duct length.

To quantify the effect of area ratio on ducted fan performance, a ‘long’ exit duct was tested with a ratio of L/h equal to 2, as the ESDU charts show this to have a relatively large region of achievable area ratios where the flow does not separate, and boundary layer growth is not detrimental to performance [9].

The length of the duct is important as longer ducts are heavier and therefore, have a lower net thrust. To analyse the impact of L/h ratio on duct performance and separation, a second ‘short’ exit duct was tested with a 50% reduction in length.

6.2 CFD Results

6.2.1 Exit Duct Area Ratio

The different exit duct geometries were first tested using CFD. The geometric area ratio is calculated using the duct geometry. To calculate the actual area ratio, the mass averaged velocity at exit was used to calculate the actual flow area at exit of the duct, Equations (14) and (15). The long exit ducts tested, $L/h = 2$, had area ratios ranging from $\sigma_{geom} = 1.00$ to $\sigma_{geom} = 2.05$ and the short exit duct tested, $L/h = 1$, had $\sigma_{geom} = 1.69$.

$$\bar{V}_x = \frac{\int V_x(r)\rho V_x(r)2\pi r dr}{\dot{m}} \quad (14)$$

$$A_{actual} = \frac{\dot{m}}{\rho \bar{V}_x} \quad (15)$$

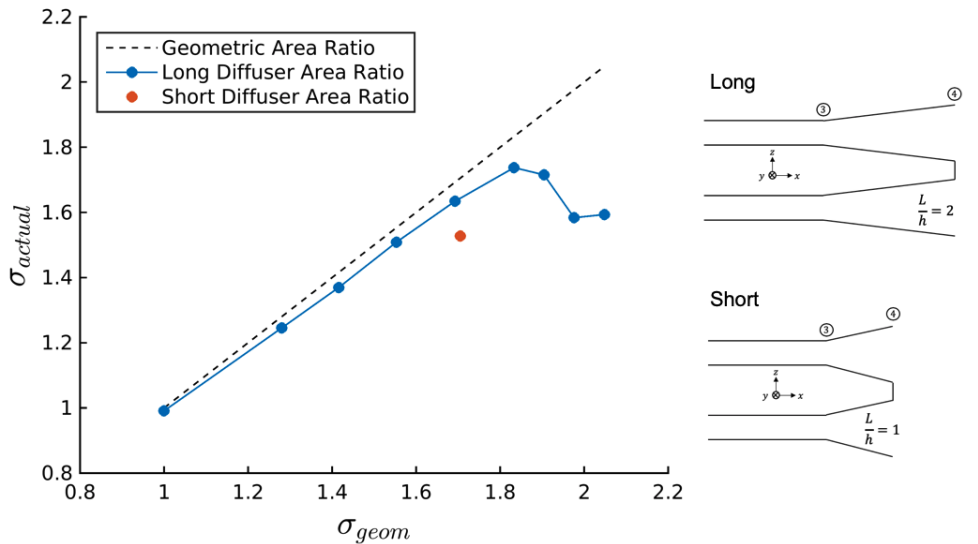
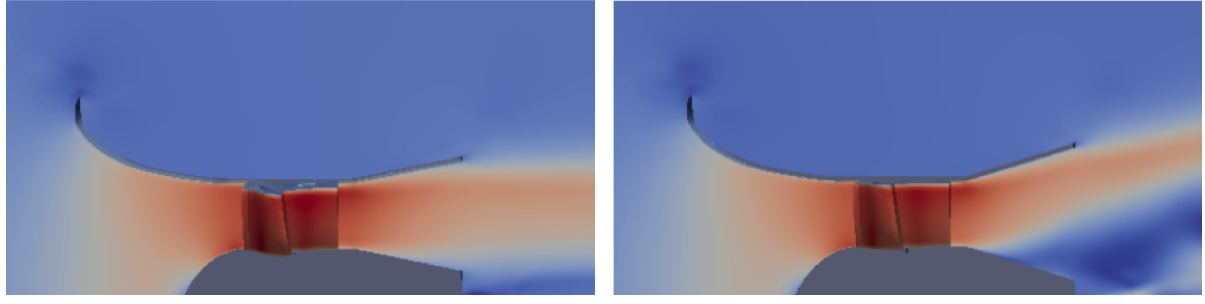


Figure 20: Actual area ratio against geometric area ratio for the exit ducts tested using CFD

Figure 20 shows that as geometric area ratio was increased, the difference between the geometric area ratio and the actual area ratio grew. At a geometric area ratio of $\sigma_{geom} = 1.69$ the percentage difference between the actual and geometric area ratio was 3.59%, whereas for the diffuser with $\sigma_{geom} = 2.05$, the percentage difference was 22.22%. A significant difference between geometric area ratio and actual area ratio suggests that the flow out of the diffuser has separated, leading to a reduction in actual flow area at exit and therefore a lower actual area ratio of the diffuser. This assumption of the flow being separated was supported by the plots of flow coefficient from the output of the CFD. Figure 21a shows the flow attached for the long diffuser with $\sigma_{geom} = 1.69$ and Fig. 21b shows the flow separating off the exit cone of the long diffuser with $\sigma_{geom} = 2.05$.



(a) Attached, long diffuser $\sigma_{geom} = 1.69$

(b) Separated, long diffuser $\sigma_{geom} = 2.05$

Figure 21: Plots of flow coefficient showing separation for a larger geometric area ratio

Figure 20 shows that appreciable separation of the long exit ducts started above $\sigma_{geom} = 1.69$. This is within 4% of the ESDU limit for separation of $\sigma = 1.63$ for a symmetrical annular diffuser with $L/h = 2$, showing that the results agree well with ESDU [9].

The short diffuser has a percentage difference between geometric area ratio and actual area ratio of 9.63%. This shows that when the length of the diffuser was halved, for the same geometric area ratio $\sigma_{geom} = 1.69$, the flow went from being attached to being separated. A larger duct angle is required for a shorter duct to achieve the same value of σ_{geom} as a long duct. This leads to more aggressive diffusion and a stronger adverse pressure gradient, causing separation.

6.2.2 Thrust Decomposition

For the ducts tested with $L/h = 2$, the non-dimensional thrust contribution of each ducted fan section is plotted in Fig. 22, where thrust is non-dimensionalised using the design axial velocity, as described in Equation (12).

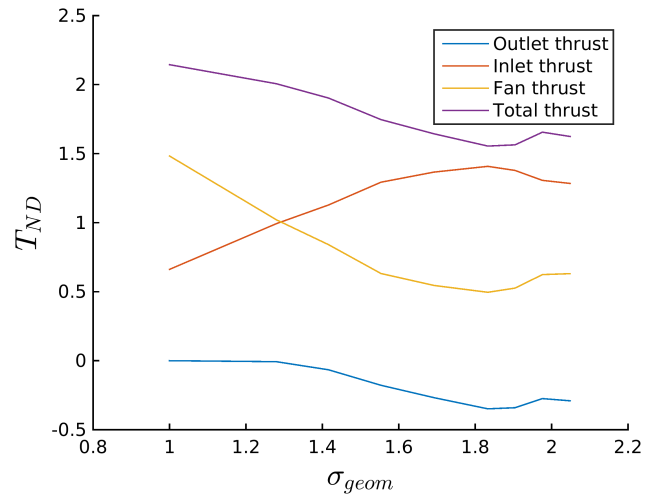


Figure 22: Non-dimensional thrust components of ducted fans tested with $L/h = 2$

Figure 22 shows that, before separation of the exit ducts above $\sigma_{geom} = 1.69$, the inlet thrust increases with area ratio. This is due to an increase in the mass flow through the fan with area ratio. As area ratio is increased, the thrust across the fan section decreases. This is because increasing the area ratio off-loads the rotor and causes the blade elements to operate at lower angles of attack [11], this also causes a reduction in the power consumed.

Equations (7), (9) and (10) for the thrust contributions of each section of the ducted fan can be simplified to calculate the theoretical, ideal contributions to thrust [11]. These can be written in terms of the area ratio using the theoretical equation for total thrust, Equations (16) to (18). Further derivation can be found in Appendix C.

$$\frac{T_{Inlet}}{T_{Total}} = \frac{\sigma}{2} \quad (16) \quad \frac{T_{Fan}}{T_{Total}} = \frac{1}{2\sigma} \quad (17) \quad \frac{T_{Exit}}{T_{Total}} = \frac{-(\sigma - 1)^2}{2\sigma} \quad (18)$$

The proportion of total thrust generated by each section of the ducted fans tested using CFD are plotted in Fig. 23. The theoretical thrust contributions for corresponding area ratios are also plotted in Fig. 23 for comparison.

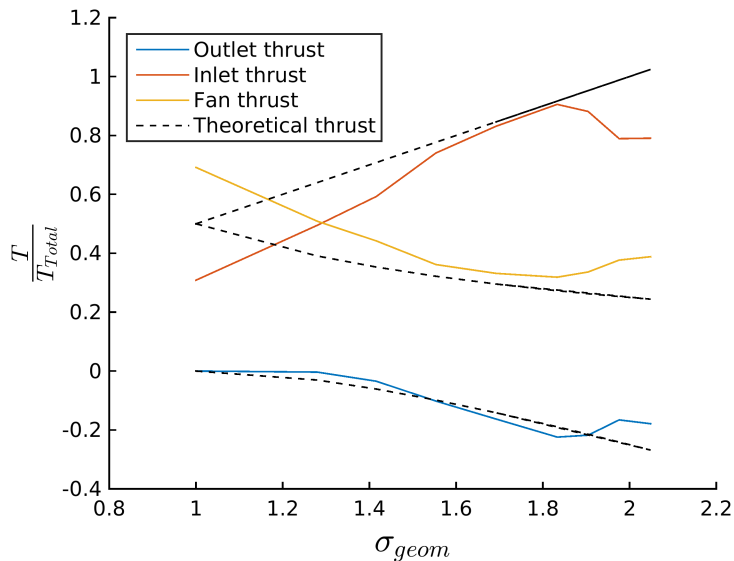


Figure 23: Proportion of total thrust of each ducted fan section for ducted fans with $L/h = 2$

Figure 23 shows that the trend of the thrust contributions agree well with the theory to the point where the ducts show appreciable separation. However, the actual values differ from theory. The proportions of total thrust for the $\sigma_{geom} = 1.69$ exit duct are shown in Table 4.

| Thrust | Theoretical Value | Actual Value | % Difference |
|-----------------------|-------------------|--------------|--------------|
| T_{Inlet}/T_{Total} | 0.845 | 0.831 | 1.66 |
| T_{Fan}/T_{Total} | 0.296 | 0.332 | 10.8 |
| T_{Exit}/T_{Total} | -0.141 | -0.163 | 15.6 |

Table 4: Comparison of theoretical and actual thrust proportions of $\sigma_{geom} = 1.69$ exit duct

The inlet thrust agrees well with theory but the fan and exit thrust proportions disagree with the theory by more than 10%. This is likely to be due to the fan not operating at its peak efficiency and the small reduction in actual area ratio due to the growth of boundary layers in the exit duct.

6.2.3 Non-Dimensional Figure of Merit

The non-dimensional figure of merit was defined in Equation (1). The power from the CFD was calculated using the mass averaged temperatures at entrance and exit of the turbomachinery section of the ducted fan, where the mass averaged value of an arbitrary flow property, Q, is defined by Equation (19).

$$\bar{Q} = \frac{\int \rho V_x(x, r) Q(x, r) dA}{\dot{m}} \quad (19)$$

$$P = \dot{m} c_p (\bar{T}_{03} - \bar{T}_{02}) \quad (20)$$

The turbomachinery of the fan was designed in a previous project for peak efficiency for a nozzle of area ratio $\sigma = 0.85$. The operating point of the fan is coupled to the diffuser and with increased diffusion the fan pressure rise and efficiency is reduced. The efficiency characteristic is shown in Fig. 24 where efficiency is calculated using Equation (21).

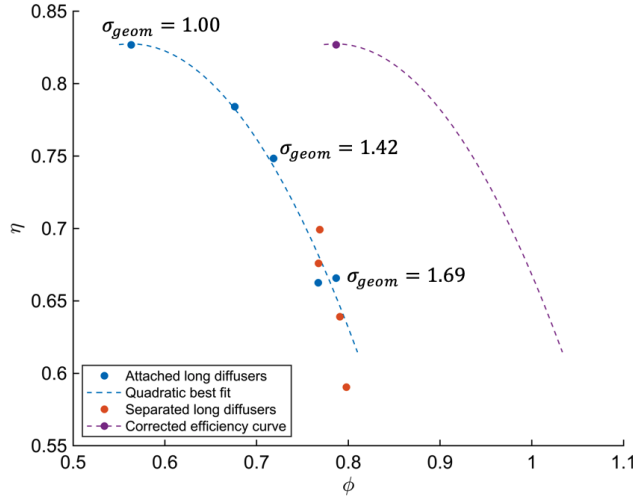


Figure 24: Isentropic fan efficiency against flow coefficient for the long exit ducts tested

$$\eta = \frac{\bar{T}_{03,s} - \bar{T}_{02}}{\bar{T}_{03} - \bar{T}_{02}} \quad (21)$$

In this work, to compare designs fairly, the fan efficiency is corrected back to the design point value no matter its operating point. This is achieved by correcting the power and figure of merit to match the value of the fan if redesigned so that the peak isentropic efficiency occurred at the new operating point, Equations (22) and (23), where η^* is the peak efficiency of the fan at its design point. The corrected efficiency curve for the $\sigma_{geom} = 1.69$ is also shown in Fig. 24.

$$P^* = P\left(\frac{\eta}{\eta^*}\right) \quad (22)$$

$$M_f^* = M_f\left(\frac{\eta^*}{\eta}\right) \quad (23)$$

The corrected figure of merit is plotted against geometric area ratio in Fig. 25 for the exit ducts tested using CFD.

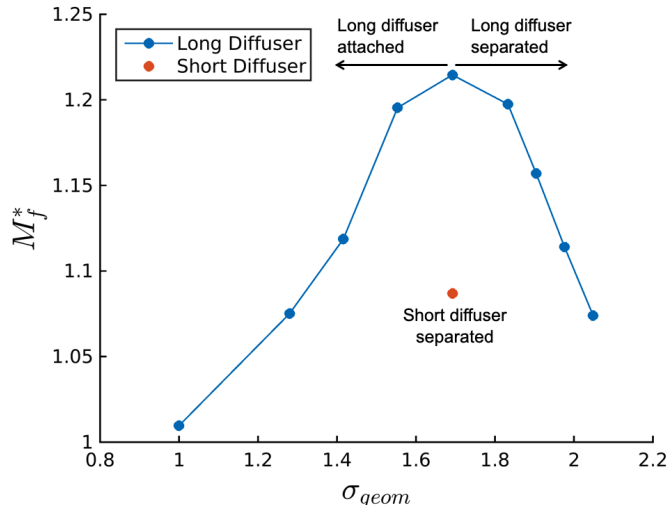


Figure 25: Figure of merit for corresponding geometric area ratios tested using CFD

Figure 25 shows that, of the 9 long exit ducts tested, the diffuser with $\sigma_{geom} = 1.69$ had the best performance. This diffuser corresponded to an exit duct angle of 10° . Above this geometric area ratio, the figure of merit decreases due to the separation of the exit ducts reducing the actual area ratio.

The corrected figure of merit is plotted against actual area ratio in Fig. 26. Section 6.2.2 showed that the total thrust reduced with increasing actual area ratio. Despite this, the figure of merit can still increase due to a reduction in power consumption.

Figure 26 shows that increasing actual area ratio increased the figure of merit up until the point where the exit ducts began to separate. After this point, even with a higher actual area ratio, the ducted fan performance reduced. For the $\sigma_{geom} = 2.05$ long diffuser, its actual area ratio was 1.60 and its figure of merit 1.06. This is similar to the figure of merit value of the long diffuser with actual area ratio of 1.25 and no separation. This shows that the separation of the $\sigma_{geom} = 2.05$ long diffuser has led to extra losses, reducing the overall performance of the fan and its figure of merit to that of a much smaller area ratio diffuser with no separation.

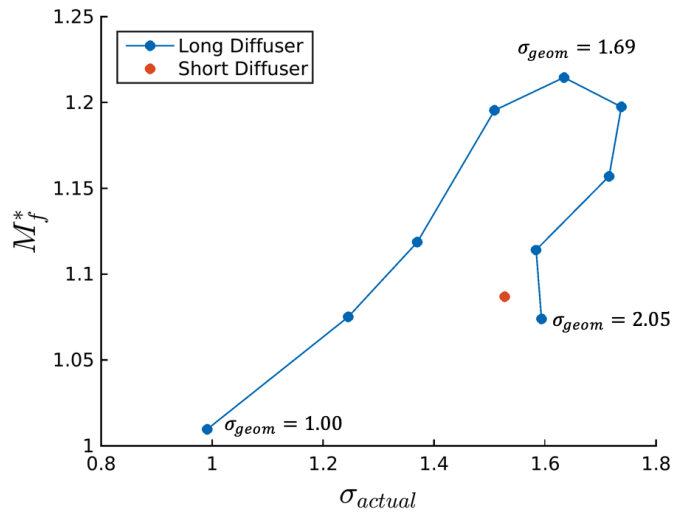


Figure 26: Figure of merit for corresponding actual area ratios tested using CFD

Decreasing the length of the $\sigma_{geom} = 1.69$ exit duct reduced the figure of merit from 1.21 to 1.09. This is due to the separation of the short exit duct and the increase in losses.

The theoretical figure of merit for a chosen area ratio was given in Equation (2). The figure of merits calculated using CFD are much smaller than that predicted by theory. For the $\sigma_{geom} = 1.69$ diffuser, theory predicts it to have a figure of merit of 1.84, whereas the figure of merit predicted using CFD is 34% less than this. This is due to two reasons, firstly the efficiency of the fan. This fan has a peak efficiency of 83%. Secondly, viscous effects in the exit duct mean that the actual area ratio is always lower than the geometric, even in the optimum case, where there is no separation, due to the growth of boundary layers.

6.3 Experimental Results

Four exit ducts were 3D printed and tested on the eVTOL rig. The diffuser with $\sigma_{geom} = 1.69$ was the highest performing exit duct and so long, $L/h = 2$, and short, $L/h = 1$, versions of this duct were printed. Long $\sigma_{geom} = 1.00$ and $\sigma_{geom} = 1.42$ exit ducts were also 3D printed to validate the results of the CFD.

6.3.1 Exit Traverse Results

The exit of each duct was traversed to show the effect of area ratio on separation. Figure 27 shows plots of stagnation pressure coefficient as defined in Equation (24). The white regions of the plots show where there is no flow and the stagnation pressure is equal to atmospheric pressure. The dashed lines outline the final geometry of the exit casing and exit cones.

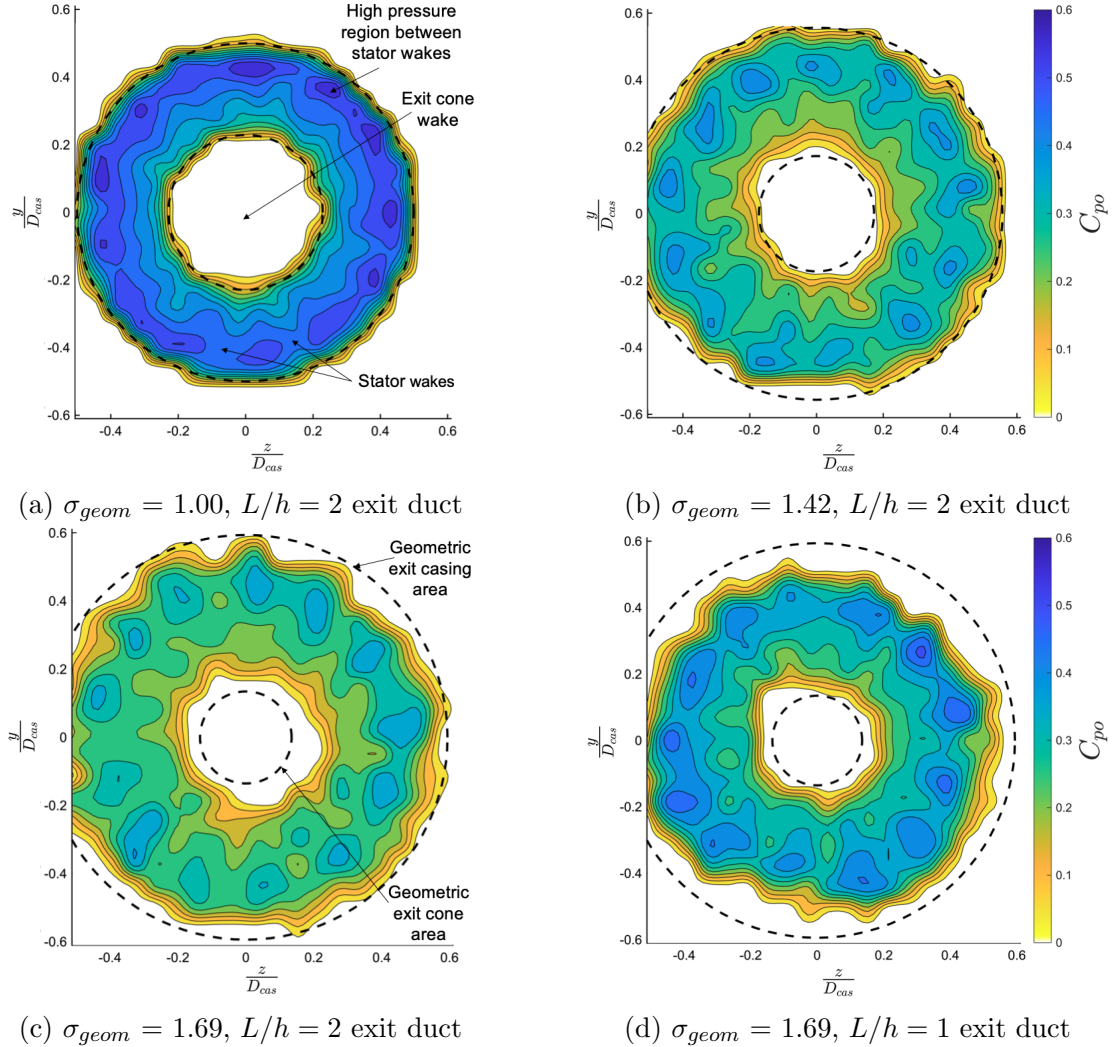


Figure 27: Traverse plots of total pressure coefficient for exit ducts tested on the eVTOL rig

$$C_{po} = \frac{p_0 - p_{atm}}{\frac{1}{2}\rho U^2} \quad (24)$$

Figure 27 shows that as the area ratio is increased, the stagnation pressure between 20% and 80% of the span reduces. The reason for this is diffusing the flow at exit increases the mass flow through the fan, changing the velocity triangles through the rotor and unloading the fan. The 13 regions of high stagnation pressure coefficient in each of the plots of Fig. 27 show the jets of flow between the 13 stator wakes. The stator wakes become more predominant as the flow is diffused and as the duct length is made shorter. This is because the stagnation pressure is non-uniform at entrance to the exit duct and diffusing the flow amplifies this further, suggesting that mixing losses from the stator blades are worse [22]. For the shorter duct, this is more predominant as there is also less time for mixing in the flow.

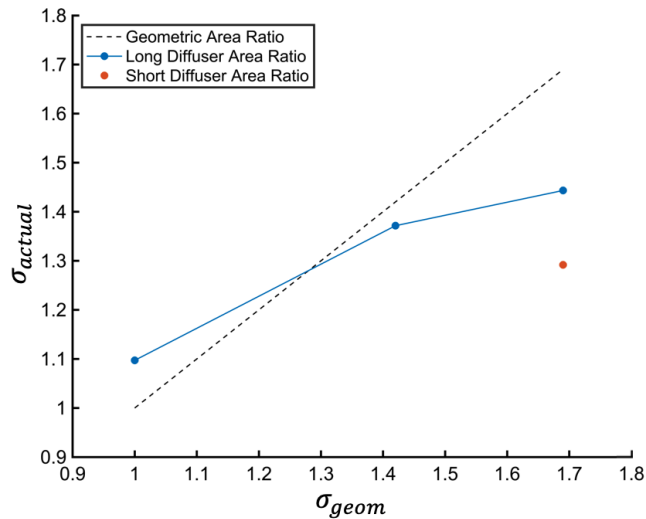


Figure 28: Actual area ratio against geometric area ratio for experimental exit ducts

Figure 28 shows actual area ratio against geometric for the exit ducts tested on the eVTOL rig. For the $\sigma_{geom} = 1.00$ exit duct, the actual area ratio is larger than the geometric area ratio. This is due to the flow being attached along the full length of the exit cone and therefore, it diffuses slightly when it exits the duct, before reaching the five-hole probe.

The difference between the actual area ratio and geometric area ratio for the $\sigma_{geom} = 1.42$ exit duct tested was 3.3% suggesting no significant separation. For the long, $\sigma_{geom} = 1.69$ exit duct, the flow has separated on the exit cone but stayed attached along the majority of the casing. This was not predicted using CFD, suggesting that CFD is conservative when it comes to separation. For the short $\sigma_{geom} = 1.69$ diffuser, the flow has separated off the casing which has subsequently helped it remain attached to the exit cone for longer. The actual flow area of the long duct at exit is 11.7% larger than the shorter duct showing that,

despite the small separation on the exit cone of the long duct, significantly less separation has occurred on the longer duct than the short duct.

6.3.2 Preliminary Results

In the next stage of the project, the figure of merit of each duct was to be measured using the instrumentation on the eVTOL rig. This would have quantitatively shown which diffuser improved the ducted fan performance the most. Results for thrust and power collected so far, at an intermediate fan speed, are tabulated in Table 5. To accurately calculate the figure of merit, the results were to be repeated at full speed and measurements taken to calculate the fan efficiency, refer to Appendix E.

| σ_{geom} | L/h | σ_{actual} | T_{Total} , N | Power, W |
|-----------------|-------|-------------------|-----------------|----------|
| 1.00 | 2.00 | 1.09 | 21.81 | 272.6 |
| 1.42 | 2.00 | 1.37 | 18.49 | - |
| 1.69 | 2.00 | 1.44 | 17.53 | - |
| 1.69 | 1.00 | 1.29 | 19.01 | 251.16 |

Table 5: Preliminary results of exit ducts tested on the eVTOL rig

The short $\sigma_{geom} = 1.69$ has a higher thrust than the $\sigma_{geom} = 1.42$ diffuser as its actual area ratio is smaller due to separation. Whilst these results do not confirm whether the performance of the increased area ratio is better or worse, it shows that increasing the area ratio of the fan has influenced the performance parameters as expected; the thrust and power are decreasing with actual area ratio and shortening the duct leads to increased separation, which is detrimental to ducted fan performance. This suggests that, if the losses from the small exit cone separation on the long $\sigma_{geom} = 1.69$ exit duct are low, this would have had the highest figure of merit out of the four exit ducts tested on the eVTOL rig.

7 The Effect of Splitter Blades on Exit Duct Length

7.1 Splitter Blade Design

The splitter was designed in 2D as a blade with zero camber. Different positioning of the blade was tested but the impact on performance was small. Therefore, the splitter blade was positioned for equal area ratio cone side and casing side, as this was the most consistent approach for adding a splitter to different exit duct geometries. Figure 29 shows the final positioning of the 2D splitter blade.

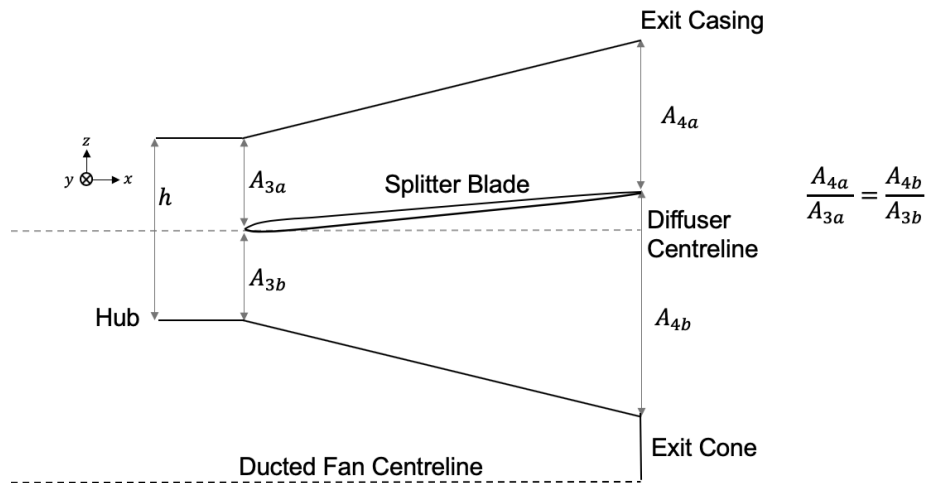


Figure 29: 2D splitter blade geometry

7.2 CFD Splitter Blade Performance

Splitters were added to the long diffuser with $\sigma_{geom} = 2.05$ and the short diffuser with $\sigma_{geom} = 1.69$. Both diffusers were separated with no splitters. In both cases the splitter blade kept the flow attached to the exit cone for longer, increasing the actual area ratio of the diffusers, as shown in Fig. 30a.

For the long diffuser with $\sigma_{geom} = 2.05$, the splitter increased the actual area ratio. However, the area ratio with the splitter was still 15.5% lower than the geometric area ratio. This suggests that the diffusion is still too aggressive and the growth of boundary layers on the long splitter blade reduce the maximum achievable area ratio. Despite increasing the actual area ratio, the addition of the long splitter reduced the figure of merit of the diffuser from 1.07 to 0.98, as shown in Fig. 30b. This is most probably due to the increased boundary layer loss being more detrimental than any increase in performance from a larger actual area ratio.

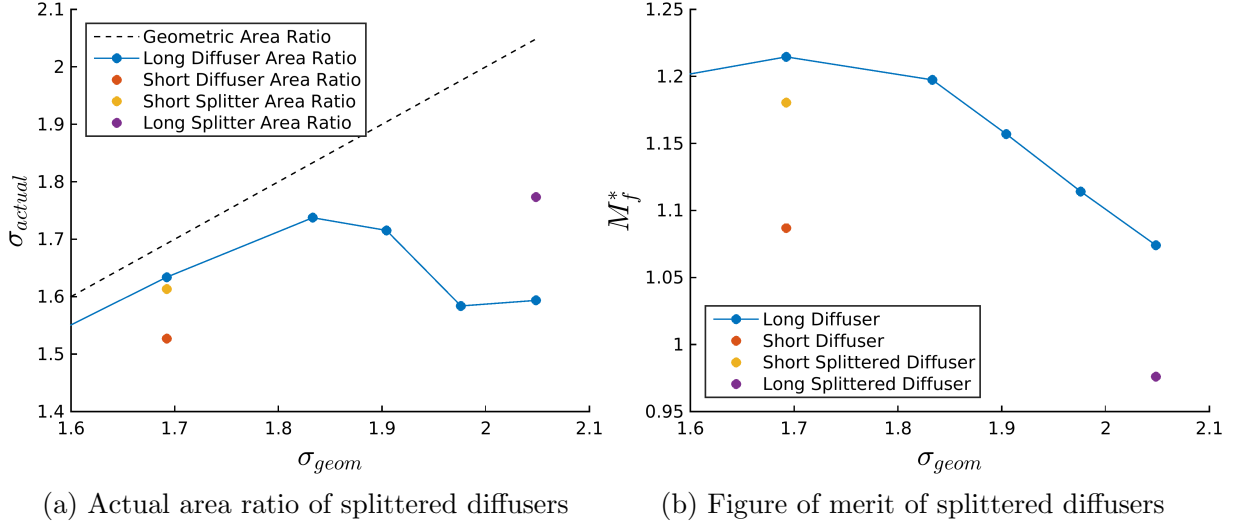
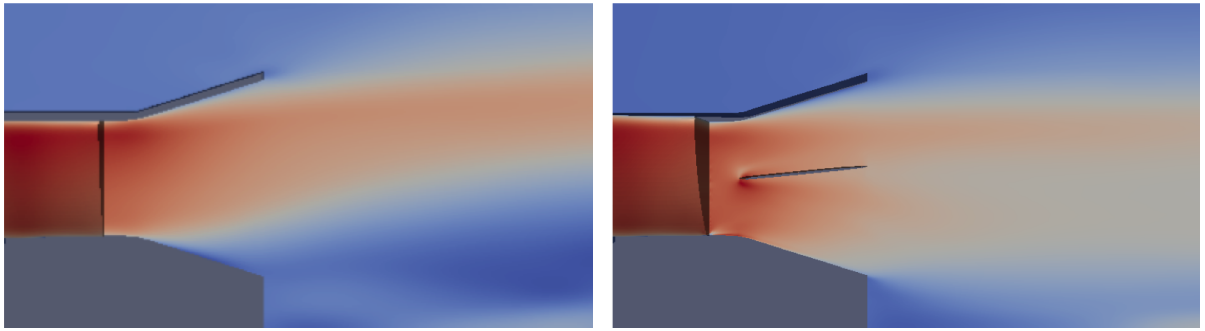


Figure 30: Influence of splitters on exit duct area ratio and figure of merit

For the short duct with $\sigma_{geom} = 1.69$, the flow was separated, as shown in Fig. 31a. With the splitter blade the actual area ratio increased by 0.08. Figure 31b shows that adding the splitter blade to the short diffuser helped the flow to stay attached. Since the splitter blade is shorter for this diffuser than the previous splitter blade, the increase in attached boundary layer loss will be less, allowing the figure of merit to increase. The addition of the splitter blade increased the figure of merit of the short exit duct by 8.26%.



(a) Short diffuser separating off the exit cone (b) Short diffuser with splitter remaining attached

Figure 31: Plots of flow coefficient for diffusers with $\sigma_{geom} = 1.69$ and $L/h = 1$

The values obtained using CFD of actual area ratio and figure of merit for the different ducts tested with $\sigma_{geom} = 1.69$ are given in Table 6.

| Exit Duct | L/h | σ_{geom} | σ_{actual} | Figure of Merit |
|-------------------------|-------|-----------------|-------------------|-----------------|
| Long diffuser | 2 | 1.69 | 1.63 | 1.21 |
| Short diffuser | 1 | 1.69 | 1.53 | 1.09 |
| Short splitted diffuser | 1 | 1.69 | 1.61 | 1.18 |

Table 6: Summary of performance of exit ducts with $\sigma_{geom} = 1.69$ tested using CFD

The values for the short, splitted diffuser are comparable with that of the long diffuser with the same geometric area ratio and no separation; the actual area ratio is 1.22% lower and the figure of merit 2.48% lower. This suggests that a splitter blade allows the duct length to be halved with minimal detrimental effect on the performance of the duct and therefore, the duct can be made lighter and have a larger net thrust. Ignoring the weight of the splitter, halving the length of the exit duct, whilst maintaining the same geometric area ratio, reduces the exit duct weight by 47.83%.

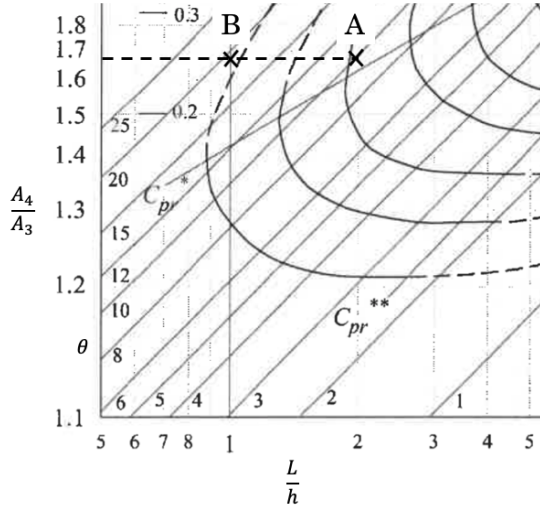


Figure 32: ESDU performance chart for symmetrical annular diffusers, adapted from [9]

Figure 32 shows how the exit duct compares to the ESDU performance charts. The C_{pr}^* line represents the optimum area ratio for a given static-pressure recovery coefficient and provides an estimation of the limit of separation of a diffuser. Point A shows the long diffuser with $\sigma_{geom} = 1.69$ very close to the limit of separation. When the length of the diffuser was halved but σ_{geom} kept at 1.69, this halved L/h causing the exit duct to move further above the limit of separation.

The addition of the splitter blade on the short exit duct causes h to half, moving the exit duct from point B to point A. However, with a splitter, the diffusing sections on both the exit casing and exit cone sides of the splitter blade are not symmetrical due to the angle of the splitter blade. ESDU 75026 provides static pressure recovery coefficient charts for three different annular diffuser geometries: symmetrical, parallel core and $\theta_i = 5^\circ$. The ESDU chart of Fig. 32 assumes a symmetrical, annular diffuser, therefore the diffuser geometry

with the splitter blade no longer aligns with this chart or the other charts produced by ESDU.

There are three important things that will determine whether the diffuser separates or not. The area ratio, the L/h ratio and the angles either side of the diffusing duct. The influence of the first two on separation is shown but the third is less well understood when the duct angles are not symmetrical.

7.3 Experimental Splitter Blade Performance

7.3.1 Traverse Results

The short diffuser with the splitter was 3D printed and tested on the eVTOL rig. To attach the circumferential splitter blade to the ducted fan, radial struts were used. The exit area of the short diffuser with the splitter was traversed and contours of stagnation pressure coefficient as defined in Equation (24) are plotted in Fig. 33b.

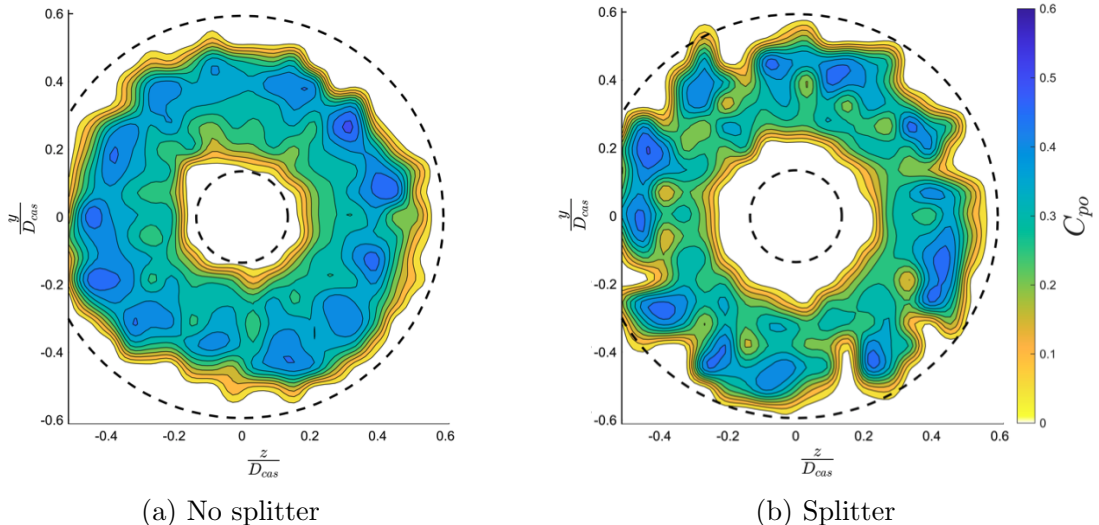


Figure 33: Exit 2D traverse plots for short $\sigma_{geom} = 1.69$ diffusers

The traverse plot of the short diffuser with no splitter blade shows that it stayed attached along the exit cone but separated on the exit casing. The addition of the splitter blade helped to keep the flow attached to the casing for longer. However, in this case the flow has now separated off the exit cone, shown by the larger white area in the centre. The actual area ratios of the $\sigma_{geom} = 1.69$ diffusers tested experimentally are tabulated in Table 7.

| Exit Duct | L/h | σ_{geom} | σ_{actual} |
|-------------------------|-------|-----------------|-------------------|
| Long diffuser | 2 | 1.69 | 1.44 |
| Short diffuser | 1 | 1.69 | 1.29 |
| Short splitted diffuser | 1 | 1.69 | 1.33 |

Table 7: Summary of performance of exit ducts with $\sigma_{geom} = 1.69$ tested on the eVTOL rig

The splitter blade tested on the rig increased the actual area ratio of the short diffuser by 3.1%, which is less than the increase predicted using CFD of 5.22%. In the next stage of the project, the splitter blade performance would have been quantified using measurements of total thrust and power from the rig to calculate the figure of merit, Appendix E. Since the splitter has increased the actual area ratio of the short diffuser, it is likely the figure of merit has also increased. With performance quantified, adjustments would then have been made to the splitter blade design to improve the exit duct performance further.

8 Sensitivity to 3D Geometry

There were two main discrepancies between the CFD and experimental results. The first being the performance of the splitter on the eVTOL rig, and the second being the side of the exit duct from which the flow separated.

8.1 Splitter Blade Performance

The addition of the splitter blade on the ducted fan tested experimentally increased the actual area ratio of the short diffuser to 1.33 whereas in the CFD it was increased to 1.61, much closer to the geometric area ratio of 1.69. This discrepancy is thought to be due to two problems which occurred when moving from the axisymmetric CFD model to the 3D flow of the ducted fan tested on the eVTOL rig. Firstly, the influence of swirl with the addition of struts and secondly, the incidence of the flow on the splitter blade.

8.1.1 Influence of Swirl and Struts

Swirl of the flow and its effect on struts was investigated as the first explanation for the discrepancy between the CFD and the experimental splitter performance. When using a circumferential splitter on the eVTOL rig, radial struts are required to hold it in place. The CFD domain is a 2D axisymmetric geometry and so the struts were not modelled. When the ducted fans were tested on the eVTOL rig, there was over 10° of swirl in the flow of the exit duct, as shown by Fig. 34.

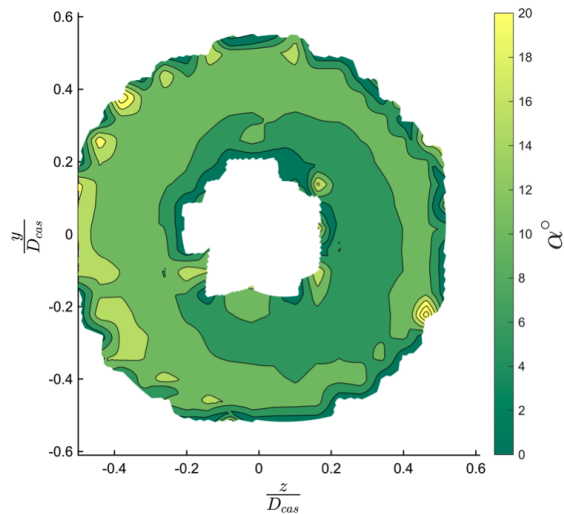


Figure 34: Swirl of experimental $\sigma_{geom} = 1.00$ exit duct, converted to polar coordinates

Significant swirl upstream of the splitter can lead to flow separating off the struts, increasing losses and affecting the duct performance. Since the struts were not modelled in the CFD, this was not predicted.

There are three ways that the interaction between swirl and struts can be minimised. First, reducing the residual swirl by redesigning the turbomachinery section of the ducted fan and re-cambering the stators. Second, the struts can be redesigned to align with the swirl. Third, the struts can be redesigned to be insensitive to swirl. The third method was adopted to improve the splitter performance as it is beneficial and robust in the swirl of any ducted fan design.



(a) Struts between exit casing and splitter blade (b) Struts between exit cone and splitter blade

Figure 35: Strut designs for the splitter blade

The splitter blade of Section 7.3.1 was supported by radial struts to the exit casing, Fig. 35a. With the aim of making the struts insensitive to swirl, a second design was tested with a reduced chord length. These struts were also placed between the splitter blade and exit cone, Fig. 35b, allowing fewer struts to be used.

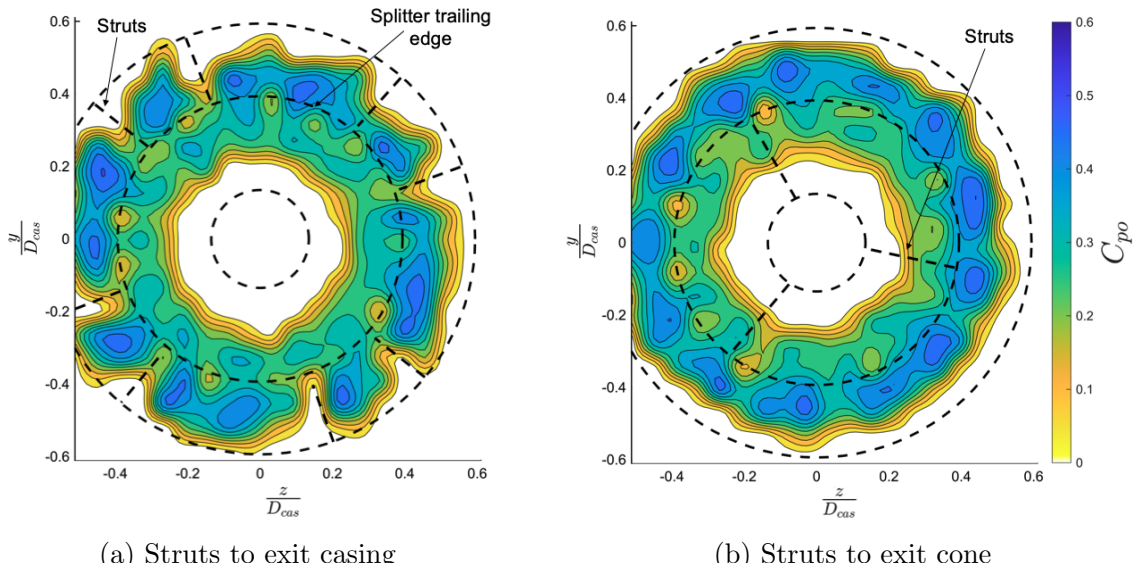


Figure 36: Exit 2D traverse plots for short, $\sigma_{geom} = 1.69$ diffusers with splitters

The exit of the second strut design was traversed and contours of stagnation pressure coefficient plotted, Fig. 36b. Comparing the two traverse plots of each strut design, the struts to the casing caused more distortion to the flow, shown by the periodic regions of separation in Fig. 36a in line with the struts. It is possible that streamwise vorticity, shed from the casing strut separations, is responsible for the distorted shape of the jet. This jet distortion is reduced in Fig. 36b, showing that reducing the chord length and using fewer struts reduces the sensitivity to swirl.

The area ratio of the second strut design was 1.32, whereas the first strut design was 1.33. This reduction is due to the flow of the second strut design separating earlier off the exit cone, despite it staying attached to the casing for longer. However, with less flow distortion, losses are likely to be reduced in the second strut design and the figure of merit likely to be higher. In the next stage of the project, the performance of each strut design would have been quantified by taking measurements for the figure of merit, see Appendix E.

8.1.2 Influence of Splitter Blade Incidence on Separation

Separation of the flow on the splitter itself was investigated as a second explanation for the discrepancy between the CFD and experimental splitter performance. CFD did not show the splitter blade to separate but the use of CFD allows cuts to be taken along the surface of the splitter blade and the blade pressure distribution to be plotted, Fig. 37, with pressure coefficient defined by Equation (25). This data cannot be obtained from the rig due to its small size. However, the pressure distribution is dominated by inviscid flow and so, the experimental blade pressure distribution should match well with that predicted using CFD [23].

$$C_p = \frac{p - \bar{p}_3}{\frac{1}{2}\rho \bar{V}_{3x}^2} \quad (25)$$

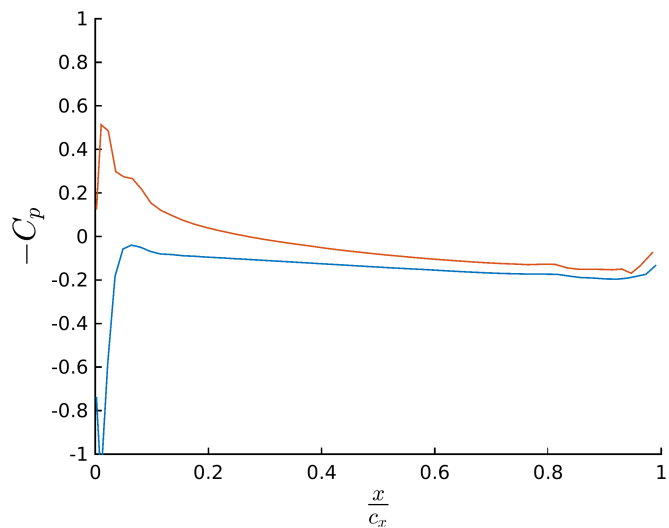


Figure 37: Pressure distribution along the splitter blade using CFD

The diffusion factor of the blade was calculated using Equation (26). Blades with large diffusion factors are prone to separation and stall [24]. From the CFD the diffusion factor of the splitter blade was calculated to be 0.45. A diffusion factor below 0.6 is often acceptable in turbomachinery design. However, the flow over the splitter blade is laminar and will have a smaller limit of diffusion than turbulent flow, this suggests that the blade is prone to separation.

$$DF = \frac{V_{max} - V_4}{V_{max}} \quad (26)$$

To investigate separation on the splitter blade of the 3D printed exit duct, flow visualisation was carried out on the splitter blade, exit cone and struts between the splitter and casing. The flow visualisation showed the flow on the exit cone side of the splitter blade to separate at the leading edge and then reattach, point A in Fig. 38a. This suggests that there could be significant pitch at exit of the stator, leading to separation on the splitter blade leading edge and a reduction in actual area ratio and figure of merit.

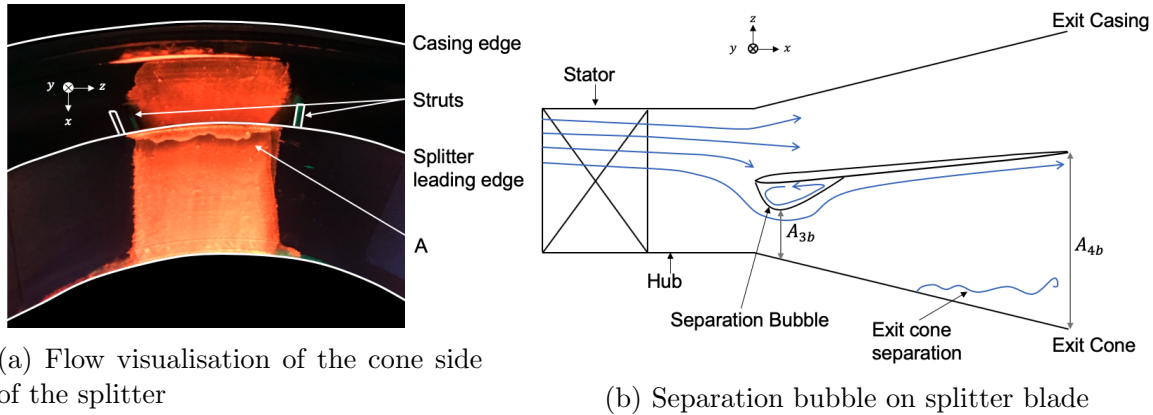


Figure 38: Separation of the splitter blade on the eVTOL rig

Other work by Hobson et al. (2001) has found that reducing Reynolds number from 640,000 to 210,000 for controlled-diffusion compressor blades in a cascade led to a laminar separation bubble [25]. The Reynolds number of the splitter blade is equal to 136,500. A separation bubble on the exit cone side of the splitter blade will reduce the flow area at this position. Therefore, the area ratio will be larger and separation on the exit cone more likely, shown schematically in Fig. 38b. This supports the findings from the traverse plot of the short splitted exit duct which showed the flow separating on the exit cone side.

In the next stage of the project, splitter blade designs with different thickness distributions were to be 3D printed and tested on the eVTOL rig to increase the incidence tolerance. Several methods have been investigated in compressor design with the aim of increasing the blade incidence tolerance. Sun et al. (2012) found increasing the leading edge diameter and wedge angle of the blade can suppress the separation of the boundary layer at off-design conditions [26]. Maffioli (2015) found that added thickness at the front of a blade can reduce

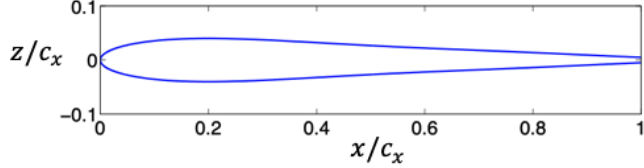


Figure 39: Thickness distribution of aerofoil with maximum thickness at $x/c_x = 0.2$ [27]

separation [27]. This front-thickened blade design is shown in Fig. 39. If this was adopted in the splitter blade design, it could potentially have greater tolerance to pitch at exit of the stator and no separation bubble.

8.2 Location of Exit Duct Separation

The results of the CFD showed that, for all separating diffusers, the location of separation was on the exit cone side. This agrees with the experimental results of the $\sigma_{geom} = 1.69$ long diffuser. However, the experimental results suggest that as diffusion is made more aggressive, as in the shorter $\sigma_{geom} = 1.69$ exit duct case, the limiting side of separation becomes the exit casing side. Hoadley (1971) has shown that when a significant swirling component is present in the inlet flow to a diffuser, this swirl can change the separation patterns in the diffuser, and it is possible for separation to occur on the opposite wall to that normally expected [28]. Since there was significant swirl in the flow of the ducted fans tested on the rig, this makes it hard to predict the location of separation.

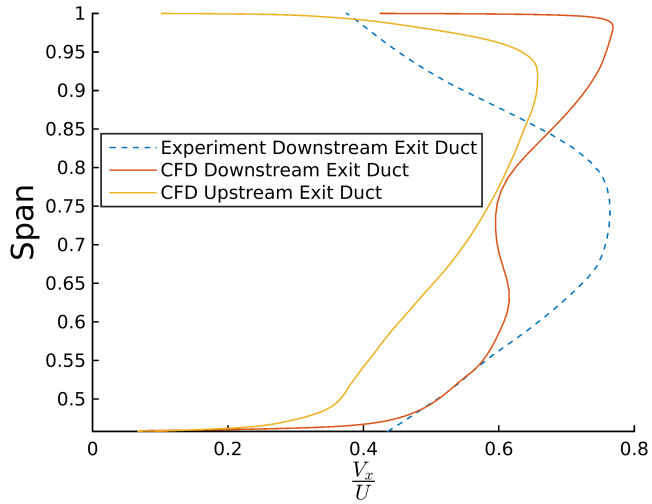


Figure 40: Flow coefficient across the span of the $\sigma_{geom} = 1$ exit duct

The discrepancy in the location of separation is also hypothesised to be due to inaccuracies in the flow coefficient distribution across the span of the exit duct predicted by the CFD. Figure 40 shows the variation in flow coefficient with span upstream and downstream of the

$\sigma_{geom} = 1$ exit duct, predicted using CFD and that obtained downstream of the $\sigma_{geom} = 1$ exit duct tested on the eVTOL rig using the five-hole probe.

CFD indicates that the flow is reduced on the exit cone side, and so this side would have been more likely to separate. When tested on the rig, the fan flow was symmetric across the span, suggesting either side of the exit duct would be equally as likely to separate.

9 Main Steps in Ducted Fan Design

When designing a ducted fan the designer must consider different contributions to performance including noise, cruise performance and material selection, and these will be dependent on the objectives of the designer. In this project, the weight and the duct geometry have been investigated. The following section characterises how these two factors can be optimised for performance in hover.

- Ensure a small adverse pressure gradient of the inlet flow by aligning the angle of the inlet with the incoming flow angle to reduce the incidence. This reduces the curvature of the flow upstream of the inlet and can be achieved by using an elliptical inlet with a large inlet diameter. The length can be reduced to minimise its weight without penalty.
- Aim for a large exit duct area ratio, whilst preventing separation. CFD shows the optimum area ratio that can be achieved to be $\sigma = 1.69$. When designing a duct for flight, an area ratio slightly below this would allow a separation margin for manoeuvring.
- Reduce exit duct weight by reducing its length and using splitters to prevent separation. Detailed analysis of splitter blade performance is critical to ensure the leading edge of the splitter blade is matched to the exit flow out of the fan and the thickness distribution is appropriate for the Reynolds number.
- It is important to analyse the influence of 3D flow effects, specifically swirl and struts on the performance of a diffuser. Reduce the chord length of struts and use as few as possible, as they can increase the uncertainty of separation.

10 Conclusions

This project demonstrated that ducted fan performance is sensitive to the duct geometry and to separation.

A ducted fan CFD model was produced, allowing detailed flow analysis. CFD is more versatile than the use of an experimental rig and allowed data to be collected which would be extremely difficult to obtain from a rig. However, CFD can struggle to predict separation accurately and test data is vital to validate the CFD findings.

Three ways of altering an ellipse inlet duct geometry to improve ducted fan performance were presented. First, shortening the length allows a reduction in weight of the ducted fan. Second, curvature upstream of the inlet duct can be reduced by using a relatively large inlet diameter. This reduces the flow incidence onto the inlet duct and reduces adverse pressure gradients, preventing separation. Third, splitters on the inlet duct were found to increase attached boundary layer losses. However, CFD did not predict separation of the inlet and so, splitter blades could be used to prevent inlet separation if present, improving performance.

Two ways of altering the exit duct geometry to improve ducted fan performance were presented. First, diffusing the fan exit flow was found to increase the ducted fan figure of merit by 21.2% when compared to a straight exit duct geometry. An optimum exit duct area ratio was found to be $\sigma = 1.69$. Second, a ducted fan exit duct can be made 47.83% lighter for a 2.48% decrease in figure of merit by reducing the length by 50%, whilst maintaining the same area ratio, and using a circumferential splitter blade to prevent separation.

Separation in two locations was shown to be detrimental to ducted fan performance and methods to prevent it were presented. First, separation of the exit duct flow on the casing or exit cone leads to increased losses and a reduction in figure of merit when compared to a duct of the same actual area ratio and no separation. This can be prevented using a splitter blade. Second, a laminar separation bubble on the splitter blade can result in a larger area ratio and separation in the diffuser. This can be prevented using splitter blade profile designs with high incidence tolerance.

It is important for the designer to understand real 3D geometry and flow features. 3D geometry can have an effect on flow separation, but methods can be adopted to limit this. This is best assessed on an experimental rig.

10.1 Future Work

Splitter Blade Design Optimisation

XFOIL, a viscous 2D solver, could be used to carry out a simulation of the splitter blade aerofoil at the Reynolds number of the flow to ensure that it does not separate [14]. Maffioli (2015) describes how front-thickened compressor blades were found to perform best in loss coefficient, deviation and rotor efficiency [27]. If tested, a tadpole shaped blade with a larger wedge angle could prevent separation and improve the splitter blade performance.

In-flight Operability

When used on an eVTOL vehicle, ducted fans need to be tolerant to cross-winds and manoeuvres. Further testing of the optimum duct design on a flying test bed or in a wind tunnel would allow the duct geometry to be improved further to increase its tolerance to separation when in flight, as well as hover. The optimum exit duct geometry for cruise is likely to be different to hover and so a variable exit duct geometry could be adopted for optimum performance in all flight stages.

For smaller scale ducted fans, with Reynolds numbers below 5×10^4 , pressure recovery decreases and the separation in the diffuser will be different [9]. Therefore, tests at smaller Reynolds numbers should be carried out for ducted fan use on micro air vehicles. The relatively large scale eVTOL rig run at low speed should give accurate results for this.

Fan Re-design

The CFD model developed in this project analysed how the ducted fan performance could be improved by using diffusers with increased area ratios. The fan section was decoupled from the exit duct to allow the exit duct performance to be analysed without changing the fan design. This was achieved by correcting the fan efficiency back to the design point value no matter its operating point. If the ducted fan was to be made for use in flight, for optimum ducted fan performance, fan redesign would need to be carried out to pair the turbomachinery section of the ducted fan with the exit duct and achieve maximum efficiency.

If the ducted fan was to be designed with variable exit duct geometry, the efficiency needs to be high in all cases. For a variable exit duct geometry, the fan characteristic, shown in Fig. 24, would be critical in ensuring that the fan is operating over an acceptable range.

Appendices

A Traverse Analysis

1D Radial Traverse

The radial traverse at inlet to the rotor enabled the velocity at rotor inlet to be calculated:

$$V_2 = \sqrt{\frac{p_0(r) - p_2(r)}{\frac{1}{2}\rho}} \quad (27)$$

The axial velocity can then be calculated using the pitch and yaw angles of the flow, measured using the five-hole probe. This allows calculation of the fan inlet mass flow.

$$\dot{m}_{in} = \int_{A_2} \rho V_{2x}(r) 2\pi r dr \quad (28)$$

The mass averaged static pressure at inlet to the rotor is given by Equation (29).

$$\bar{p}_2 = \frac{\int_{A_4} \rho V_{2x}(r) p_2(r) 2\pi r dr}{\dot{m}} \quad (29)$$

The area averaged axial velocity is given by Equation (30).

$$V_{2x} = \frac{\dot{m}}{\rho \pi (r_{cas}^2 - r_{hub}^2)} \quad (30)$$

2D Traverse

The exit traverse of each duct design provided data to calculate the mass flow rate through the fan using Equation (31).

$$\dot{m}_{out} = \int_{A_4} \rho V_{4x}(y, z) dy dz \quad (31)$$

Using continuity this should be equal to \dot{m}_{in} . The mass averaged axial component of the jet velocity is calculated using Equation (32).

$$\bar{V}_j = \frac{\int_{A_4} \rho V_{4x}(y, z) V_{4x}(y, z) dy dz}{\dot{m}} \quad (32)$$

The mass averaged stagnation pressure at exit is calculated using Equation (33).

$$\bar{p}_{04} = \frac{\int_{A_4} \rho V_{4x}(y, z) p_{04}(y, z) dy dz}{\dot{m}} \quad (33)$$

B Integration of Pressure Forces

The block domain of the ducted fan is shown in Fig. B.1. As discussed in Section 4.1, the ducted fan was split into three control volumes to split the thrust into its respective components and evaluate the performance of each ducted fan section separately. Two methods were used to calculate the thrust, the first being the steady flow momentum equation as discussed in Section 4.1 and the second being integration of pressure forces along the ducted fan surfaces.

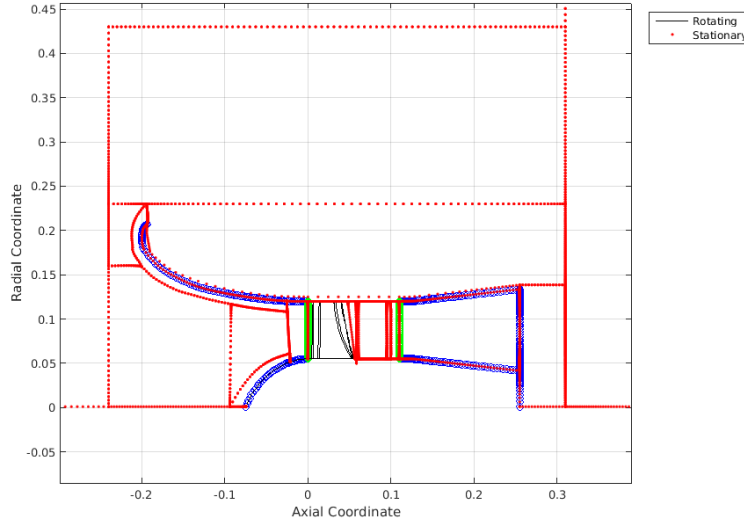


Figure B.1: Ducted fan block 2D domain with blocks in red and control volumes in blue and green

Cuts along surfaces can be made in the CFD output, where each cut is made up of N nodes and $N-1$ surfaces, assumed to be infinitesimally small. Equations (34) to (38) show how static pressure is integrated numerically along the cuts in the CFD. The same process applies for parameters other than static pressure and it can also be used for the measurements from the static pressure tappings along duct surfaces on the rig.

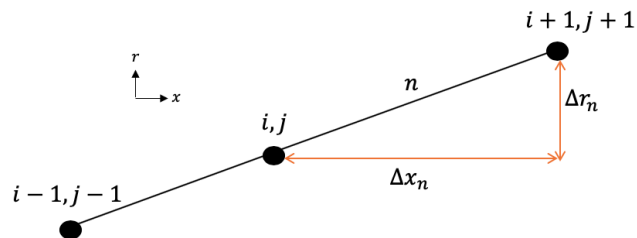


Figure B.2: Integration of flow properties along cuts from CFD output

The value of static pressure acting normal to the surface is given by the average value of the nodes either side, Equation (34).

$$p_n = \frac{(p_{i,j} + p_{i+1,j+1})}{2} \quad (34)$$

$$r_n = \frac{(r_j + r_{j+1})}{2} \quad (35)$$

$$\Delta r_n = |r_{j+1} - r_j| \quad (36)$$

$$\Delta A_n = 2\pi r_n \Delta r_n \quad (37)$$

The contribution to the thrust is then found by summing over all the nodes:

$$T = \sum_{n=1}^{N-1} p_n \Delta A_n \quad (38)$$

The thrust of a duct surface is due to the difference in pressure either side. On the experimental rig, the static pressure tappings on the inside duct surface measure gauge pressure directly. When using CFD, the absolute static pressure is extracted from the cuts. This is converted to gauge pressure when calculating the surface pressure forces of the ducted fan since, in hover, the pressure is atmospheric on the outside surface of the duct. The direction the surface pressure force acts must then be considered to determine the final thrust contribution.

C Thrust Decomposition

Equations (16) to (18) for the theoretical thrust contribution from each ducted fan section in terms of the exit duct area ratio can be derived using simple momentum theory and flow assumptions. The flow velocity through the fan is assumed axial and constant, V_x . The flow out of the exit duct, V_j , is also assumed to be axial with straight and parallel streamlines. With these assumptions, the total thrust of the fan is given by Equation (39).

$$T_{Total} = \dot{m}V_j \quad (39)$$

From continuity across the exit duct of the fan, the total thrust can be written in terms of the exit duct area ratio, Equation (42).

$$\rho V_x A_{pass} = \rho V_j A_4 \quad (40)$$

$$\rightarrow \sigma = \frac{V_x}{V_j} \quad (41)$$

$$T_{Total} = \frac{\rho A_{pass} V_x^2}{\sigma} \quad (42)$$

Assuming no losses across the inlet duct and using Bernoulli, the control volume analysis equation for inlet thrust, Equation (7), can be simplified to give the theoretical inlet thrust, Equation (43).

$$T_{Inlet} = \dot{m}V_x - \frac{1}{2}\rho V_x^2 A_{pass} = \frac{1}{2}\dot{m}V_x \quad (43)$$

Assuming constant axial velocity across the fan, Equation (9) for the control volume analysis fan thrust can be simplified to give Equation (44).

$$T_{Fan} = (p_3 - p_2)A_{pass} \quad (44)$$

The inlet stagnation pressure is equal to atmospheric, giving Equation (45) using Bernoulli. The outlet static pressure is equal to atmospheric giving Equation (46) using Bernoulli and assuming no losses across the exit duct.

$$p_2 = p_{atm} - \frac{1}{2}\rho V_x^2 \quad (45)$$

$$p_3 + \frac{1}{2}\rho V_x^2 = p_{atm} + \frac{1}{2}\rho V_j^2 \quad (46)$$

Using Equations (45) and (46), the fan and exit thrust equations can then be simplified to give Equations (47) and (48).

$$\rightarrow T_{Fan} = \frac{1}{2}\rho \left(\frac{V_x}{\sigma}\right)^2 A_{pass} \quad (47)$$

$$\rightarrow T_{Exit} = -\frac{1}{2}\rho A_{pass}(\sigma - 1)^2 \left(\frac{V_x}{\sigma}\right)^2 \quad (48)$$

Dividing Equations (43), (47) and (48) by Equation (42) gives the theoretical thrust contributions in terms of area ratio.

D Risk Assessment

The risk assessment conducted at the start of this project ensured that both the computational and experimental methods were carried out with safe practices. Regular breaks were taken to reduce eye strain from looking at a computer for long periods of time. The two risks were noise and the event of blade-off during the running of the eVTOL rig. These risks were reduced by not running the rig for prolonged periods of time to reduce heating effects and ensure no rubbing of the blading. Also, safety glasses and ear defenders were worn at all times.

E COVID-19 Disruption

Due to the ongoing Coronavirus pandemic, on Friday 20th March, all University buildings and research laboratories were closed to students and staff. The closure of the Whittle Laboratory had significant impact on the completion of the project, as the remaining work required access to the eVTOL rig. Details of the remaining work are given below with estimated time scales provided in Figure E.1.

Splittered inlet: As described in Section 5.1.2, two inlets were tested on the eVTOL rig. Inlet 3 was thought to be separated. This was to be analysed further using static pressure tappings along the inlet surface. Also, a splitted inlet was to be 3D printed with the aim of reducing inlet separation. Radial inlet traverses were not required as the mass flow was to be calculated using the calibration factor described in Section 3.2.3.

Rig measurements for each exit duct printed: Six exit ducts had been 3D printed over the duration of the project and their exit areas traversed. To quantify their performance, further measurements were required, these had been set up but were yet to be taken. First, total thrust and power to calculate figure of merit. These would have been recorded using the load cell and power box. Second, recording pressure transducer measurements of the static pressure tappings at upstream and downstream of the fan and along the duct surfaces. This was required for two reasons. First, to calculate the efficiency of each duct design for calculation of the corrected figure of merit. Second, to analyse the thrust breakdown of each duct design.

Exit splitter blade adjustments: As described in Sections 7.3 and 8.1, two splitted exit ducts had been 3D printed and traversed. To further improve the splitted exit duct performance, a third design with a tadpole shaped splitter blade was to be printed and tested on the eVTOL rig.

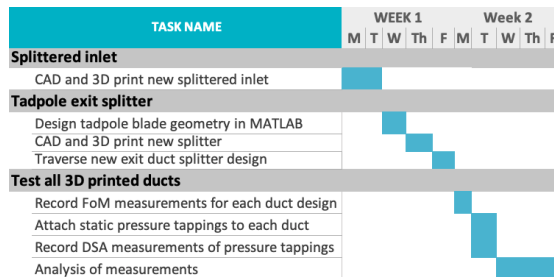


Figure E.1: Timeline of remaining laboratory work to be completed

With no access to a 3D printer or the eVTOL rig, the above were not practicably achievable. Assumptions about experimental duct performance were made from preliminary data. The report was adapted to include more CFD analysis, as this could be completed remotely.

References

- [1] Shakhatreh, H., Sawalmeh, A., (2018) *Unmanned Aerial Vehicles: A Survey on Civil Applications and Key Research Challenges*
- [2] (2019) *Unmanned Aerial Vehicles (UAV) Market: Global Forecast to 2025*, MarketsandMarkets
- [3] Department for Business, Energy & Industrial Strategy, (2018) *UK Greenhouse Gas Emissions, Provisional Figures*, National Statistics, OGL
- [4] Nicolas Zart, (2018) *Can Flying Cars Save the Environment?*, CleanTechnica, accessed: 01/05/2020
- [5] Verticle Flight Society, Aurora Flight Sciences Pegasus PAV, <https://evelot.news/aircraft/aurora/>, accessed: 23/11/2019
- [6] Lipera, L., (2001) *The Micro Craft iSTAR Micro Air Vehicle: Control System Design and Testing*, American Helicopter Society International, Inc.
- [7] Glegg, S. A. L., Devenport, W. J., (2017) *Aerocoustics of Low Mach Number Flows*, Elsevier
- [8] Akturk, A., (2014) *Lip Separation and Inlet Flow Distortion Control in Ducted Fans Used in VTOL Systems*, ASME Turbo Expo
- [9] I.C. Remfry et al., (1998) *Performance of Circular Annular Diffusers in Incompressible Flow*, ESDU 75026.
- [10] Hiller Aircraft Corporation, (1960) *Comparative Performance Charts for Ducted Propellers*, Defence Technical Information Centre
- [11] Pereira, J. L., (2008) *Hover and Wind-Tunnel Testing of Shrouded Rotors for Improved Micro Air Vehicle Design*
- [12] Chehhat, A., Si-Ameur, M., Boumeddane, B., Serie, E., Boulahrouz, S., (2016) *Numerical investigation of diffuser solidity effect on turbulent airflow and performance of the turbocharger compressor*, University of West Bohemia, Pilsen
- [13] Clark, C., Pullan, G., Curtis, E., (2016) *Secondary Flow Control in Low Aspect Ratio Vanes using Splitters*, Whittle Laboratory
- [14] Drela M., (1989) “XFOIL: An Analysis and Design System for Low Reynolds Number Airfoils”, Mueller T.J. (eds) *Low Reynolds Number Aerodynamics. Lecture Notes in Engineering*, vol 54. Springer, Berlin, Heidelberg

- [15] Goodhand, M. N., Miller, R. J., (2012) *The Impact of Real Geometries on Three-Dimensional Separations in Compressors*, Vol 134, ASME.
- [16] Brandvik, T., and Pullan, G., (2010) *An Accelerated 3D Navier Stokes Solver for Flows in Turbomachines*, ASME J. Turbomach., 133(2)
- [17] Denton, J.D., (2017) *Multistage Turbomachinery Flow Calculation Program MULTALL OPEN*, ASME
- [18] Denton, J. D., (2010) *Some Limitations of Turbomachinery CFD*, Whittle Laboratory
- [19] Dominy, R.G., Hodson, H. P., (1992) *An Investigation of Factors Influencing the Calibration of Five-hole Probes for Three-Dimensional Flow Measurements*, Journal of Turbomachinery, ASME.
- [20] Grimshaw, S. D., Taylor, J. V., (2016) *Fast Settling Millimetre-Scale Five-Hole Probes*, Proceeding of ASME Turbo Expo 2016, Seoul.
- [21] Dunkley, M. J., (1998) *The Aerodynamics of Intermediate Pressure Turbines*, Ph.D. thesis, University of Cambridge, Department of Engineering
- [22] Denton, J. D., (1993) *Loss Mechanisms in Turbomachines*, IGTI Scholar Lecture, Whittle Laboratory
- [23] Cumpsty, N.A., (1989) *Compressor Aerodynamics*, Longman Scientific & Technical
- [24] Lieblein, S., Broderick, R.L., (1953) *Diffusion Factor for Estimating Losses and Limiting Blade Loading in Axial-Flow Compressor Blade Elements*, NACA RM 53001
- [25] Hobson, G. V., Hansen, D. J., Schnorenberg, D. G., Grove, D. V., (2001) *Effect of Reynolds Number on Separation Bubbles on Controlled-Diffusion Compressor Blades in Cascade*, Department of Aeronautics and Astronautics
- [26] Hao Sun, Jun Li & Zhenping Feng., (2012) *Investigations on Aerodynamic Performance of Turbine Cascade at Different Flow Conditions*, *Engineering Applications of Computational Fluid Mechanics*, 6:2, 214-223
- [27] Maffioli, A., Hall, C., (2015) *Aerodynamics of Low Reynolds Number Axial Compressor Sections*, 53rd AIAA Aerospace Sciences Meeting
- [28] Hoadley, D., (1971) *Boundary Layer Development in an Annular Diffuser*, Salford University